TEXAS A&M UNIVERSITY
MECHANICAL ENGINEERING DEPARTMENT
TURBOMACHINERY LABORATORY
TRIBOLOGY GROUP

THERMAL EFFECTS ON PAD DEFORMATIONS AND TILTING-PAD JOURNAL BEARING PERFORMANCE

Research Progress Report to the TAMU Turbomachinery Research Consortium

TRC-B&C-04-2016

By

Luis San Andrés
Mast-Childs Chair Professor
Principal Investigator

Behzad Abdollahi
Graduate Research Assistant

May 2016

EXECUTIVE SUMMARY

In moderately loaded to heavily loaded TPJBs (>1.7 MPa specific load), pad surface deformations due to both mechanical pressure and thermally induced stresses affect the operating film thickness, thus producing a bearing performance with excessive temperature rises and a likely drop in damping force coefficients. These deformations effectively change the pad curvature and increase its machined preload. This work extends earlier analyses in Refs. [1, 2, 3] to include a thermo-elasto-hydrodynamic model (TEHD) coupling the film pressure generation to the pads' structural mechanics and including pivot elastic displacements, both due to pressure and temperature changes.

The authors performed a thorough thermo-elasticity analysis of typical bearings pads subject to thermal gradients and used a commercial finite element (FE) software to calculate 3D pad deformation fields. The theoretical analysis along with physically sound assumptions led to a simple formula for prediction of the thermally induced deformation as a function of the temperature difference between the inner and back surfaces, both circumferentially averaged. The simple equation delivers results in agreement with the FE model for a number of cases. The simplicity of the model allowed its implementation in the existing predictive tool (XLTPJB®) avoiding a cumbersome iterative procedure and complexity.

Predictions are benchmarked against test data for two distinctive bearings. In the first case, Hagemann et al. [4] measure the dynamic and static characteristics of a large size (shaft radius of 0.5 m) 5 pad TPJB with load between pad (LBP) configuration under heavy loads (specific loads of 1 to 2.5 MPa). The current TEHD model predicated the temperature of pad inner surface, hydrodynamic pressure, and film thickness with a good agreement to the test data. The TEHD model reduces the discrepancy of thermo-hydrodynamic (THD) prediction and test data for peak pressure by 14%, maximum temperature by 11%, and film thickness by 56%. A $[K,C,M]$ analysis from the current model showed to excellent agreement between predictions and test data.

The second case from Coghlan and Childs [5, 6, 7] studies the effect of various direct lubrication methods on the performance of a 4 pad spherical seat TPJB with load between pad configuration under specific loads between 0.7 and 2.9 MPa and surface speeds between

38 and 85 m/s. The predicted pad inner surface temperatures were consistently larger (no more than 18% difference) than the measured ones. The predicted hot clearances were closely predicted with maximum difference of 6% for a specific load of 2.9 MPa and various shaft speeds. Predicted direct stiffness had a very good agreement with the test data, with a maximum difference of 27%. The TEHD model improves THD predictions for stiffness coefficients, especially at lower specific load (0.7 MPa). The predicted direct damping coefficients were consistently smaller than the measured ones for analysis. The predictions from TEHD model differed with the test data in a range between 27% and 52%.

Including mechanical and thermally induced deformation of the pad along with thermal expansion of shaft and housing increases peak hydrodynamic pressure and maximum film temperature; however, it reduces the minimum film thickness, bearing clearance, and journal eccentricity along the load direction. Pad thermally induced deformations increase the pad clearance due to the pad thermal warping and reduce the bearing clearance due to thermal expansion of pad, shaft, and housing. Thus, increasing the pad preload during the operation.

CONTENTS

LIST OF FIGURES

LIST OF TABLES

NOMENCLATURE

C_b	Bearing radial clearance [m]
C_p	Pad radial clearance [m]
C'_b	Estimated hot bearing radial clearance [m]
C'_p	Estimated hot pad radial clearance [m]
C_{xx}, C_{yy}	Bearing direct damping coefficients in horizontal and vertical directions [N·s/m]
C_{xy}, C_{yx}	Bearing cross coupled damping coefficients [N·s/m]
D	Shaft diameter [m]
E	Material elastic modulus [N/m^2]
e	Journal eccentricity [m]
G	Material shear modulus [N/m]
h	Heat transfer coefficient [W/m^{2}K]
H	Fluid film thickness [m]
K_{xx}, K_{yy}	Bearing direct stiffness coefficients [N/m]
K_{xy}, K_{yx}	Bearing direct stiffness coefficients [N/m]
L	Bearing length [m]
N	Journal rotational speed [RPM] $N = \Omega\pi/30$
m	Bearing preload [-], $m = 1 - C_b/C_p$
p	Pressure field on pad surface [Pa]
Q	Lubricant flow [LPM]
R_b	Bearing radius [m]
R_{back}	Pad outer surface radius [m], $R_{back} = R_s + t + C_p$
R_h	Housing inner radius [m]
R_p, R_{in}	Pad inner surface radius [m], $R_{in} = R_p = R_s + C_p$
R_s	Shaft outer radius [m]
T	Fluid film average temperature [°K]
$\bar{T}$	Circumferentially averaged temperature in pad [°K]
T_{ref}	Reference (cold) temperature [°K]
T_{in}	Pad inner surface temperature [°K]
$\bar{T}_{in}$	Average pad inner surface temperature [°K]
T_{out}	Pad outer surface temperature [°K]
$\bar{T}_{out}$	Average pad outer surface temperature [°K]
T_{sump}	Oil sump temperature [°K]
T_{supply}	Supply (inlet) oil temperature [°K]
t	Pad thickness [m]
U, V, W	Bulk flow velocities [m/s]
u	Pad thermal deformation along radial direction [m]
v	Pad thermal deformation along circumferential direction[m]
W	Load [N]
$W/(LD)$	Specific load [Pa]
ΔR_h	Housing thermal expansion [m]
ΔR_s	Shaft thermal expansion [m]
δ_p	Pad tilt angle [rad]

η_{pivot}	Pad transverse displacement [m]
ξ_{pivot}	Pad radial displacement [m]
θ_{pad}	Pad arc length [rad]
θ_{pivot}	Angle from pad pivot to pad leading edge [rad]
θ_p	Pivot angular position starting from $-x$ axis [rad]
Φ	heat flow [W/m^2]
ϕ	Attitude Angle [deg]
Ω	Shaft angular speed [rad/s]
ω	Excitation frequency [rad/s]
$\sigma_r, \sigma_{\hat{\theta}}$	Normal strain in pad local coordinate [-]
$\tau_{r\hat{\theta}}$	Shear stress in pad local coordinate [-]
$\varepsilon_r, \varepsilon_{\hat{\theta}}$	Normal strain in pad local coordinate [-]
$\gamma_{r\hat{\theta}}$	Shear strain in pad local coordinate [-]
μ	Lubricant viscosity [mPa·s]

Subscripts

back	Pad back (outer) surface
h	Housing
in	Pad inner surface
sump	Region enclosed by back of the pad and bearing housing
s	Shaft
supply	Supply (inlet) oil

Coordinate Systems

(x, y, z)	Cartesian coordinates, origin at bearing center
(r, θ, z)	Cylindrical coordinates, origin at bearing center
$(r, \hat{\theta})$	Pad local polar coordinates, origin at pivot location on pad inner surface

Abbreviations

EHD	Elastohydrodynamic
ID	Inner Diameter
OD	Outer Diameter
LBP	Load between Pads
LOP	Load on Pad
TPJB	Tilting Pad Journal Bearing
TEHD	Thermoelastohydrodynamic, includes pressure and thermally induced deformations
THD	Thermohydrodynamic
RHS, LHS	Right and left hand side

INTRODUCTION

Tilting-Pad Journal Bearings (TPJB) have received substantial attention towards their improved design and analysis methods due to their advantage in rotordynamic stability when compared to rigid surface bearings. With the continuous improvement of turbomachines, TPJBs need to withstand heavier loads while operating at higher surface speeds. Accurate predictions of bearing stiffness and damping coefficients are paramount to the dynamics of a rotating machine. In addition, an energy efficient TPJB would operate with a lower lubricant flow while still operating with cold oil temperature.

In a hydrodynamic fluid film bearing, the dominant flow is shear driven by the spinning journal which enables it to carry a load. The load carrying capacity is strongly dependent on the fluid viscosity, which is a strong function of the film temperature that raises due to the mechanical shear power loss. Thus, an ideal bearing design strives to minimize the power loss without demanding excessive lubricant supply flow. Moreover, in heavily loaded bearings the mechanical deformation of the bearing elements (i.e. pads, shaft, and housing) due to both pressure and temperature greatly affects the overall bearing performance by changing the operating pad clearance and film temperature.

1. REVIEW OF PAST WORK

In 1980, Ettles [8] develops a thermoelastohydrodynamic (TEHD) analysis for TPJBs. Ettles includes the pad deformations using a one-dimensional beam theory, and calculates the deflected radius of the pad as a function of load distribution and temperature difference across the pad thickness. To find the temperature difference across the pad thickness, Ettles assumes that only a portion of the mechanical power loss is carried away by the flowing lubricant, and the rest is conducted through the pad and journal. The author concludes that including these deformations in the analysis improves the agreement with experimental measurements, reducing the predicted bearing damping and increasing the imbalance response amplitude.

In 1983, Ferron et al. [9] compare measurements of bush internal surface temperature (within 0.5 mm to the bearing wall), film pressure, and journal eccentricity on a plain journal bearing to predictions from a three-dimensional physical model that finds the pressure field and temperature distribution in the film, shaft, and bush. Predictions of pressure field show good agreement with the measurements. However, film temperature predictions are generally lower than the measured magnitudes. The authors note a large discrepancy on the operating journal eccentricity, and conclude that thermally induced deformations of both shaft and bush and dissimilar thermal expansion due the to their different material must be considered in modeling journal bearings.

Three years later, Boncompain et al. [10] extend their early work to study thermal effects in more detail, accounting for the thermoelastic induced displacements of the shaft and bush. The authors calculate axisymmetrical shaft expansion as an increase in shaft radius, and bush thermoelastic displacements in the mid-plane of the bearing by a two-dimensional finite element method. Boncompain et al. assume that thermal deformations only change the radial clearance and journal eccentricity, and modify the film thickness based on the new radial clearance and journal eccentricity in an iterative manner. The modified film thickness, alters the temperature and pressure fields, and the process stops when, on the boundary between the film and bush, the difference of temperature and pressure between two successive iterations is less than 0.1 percent.

In 1987, Lund and Pedersen [11] develop an approximate thermoelastohydrodynamic (TEHD) method to avoid the high computation time needed for a full TEHD analysis. The approximate method assumes that the pad expansion modifies the clearance along the radial direction only. The method incorporates an implicit contribution of thermally induced deformations based on an average temperature difference across the pad thickness. However, the authors do not include the thermal expansion of either the journal or the bearing housing in the analysis. As per the mechanical deformations, Lund and Pedersen assume that the pad is a curved beam; a pressure distribution acts as a bending moment to deform the pad and changes its clearance. Also, the pivot stiffness and equilibrium force determine the radial motion of the pad. By including the thermal and mechanical deformations of the pad, Lund and Pedersen note a decrease in bearing stiffness, damping, and load carrying capacity of which the damping is the most evident. Finally, the authors determine that pivot flexibility alone reduces the mentioned characteristics as much as thermal and mechanical deformations.

In 1989, Brugier and Pascal [12] study the thermal and mechanical deformation of pads and pivots for a large sized TPJB (shaft diameter of 0.75 m and bearing length of 0.56 m). Their TEHD model includes thermal effects in the lubricant as well as pad and pivot deformations using a general structural mechanics program. The deformations are due to both hydrodynamic pressure and thermal gradient in the pads. Axially-averaged thermal and mechanical deformations modify the film thickness . The authors observe that including mechanical deformations alone reduces the film temperature; however, when including both thermal and mechanical deformations, the temperature profiles only slightly change. Brugier and Pascal believe that including the mechanical and thermally induced deformations reduces the minimum film thickness and the maximum pad temperatures slightly. On the other hand, the authors conclude that including deformations reduces the bearing damping coefficient between 10% and 25%, and increases the bearing stiffness coefficient for small loads (specific load between 1.1 MPa and 1.9 MPa) while reducing it for large loads (specific load between 1.9 MPa and 4.7 MPa). The

authors explain the stiffness coefficient behavior by primarily pressure deformation for large loads, and primarily temperature deformation for small loads.

In 1990, Wilcock and Booser [13] investigate the thermal behavior of TPJBs by including heat transfer from fluid film to the shaft and pad, and thermal and pressure deformation of the pad. The model assumes either no net heat transfer to the shaft or a constant shaft temperature. The back of the pad and the leading and trailing edges are exposed to calm lubricant at the cavity temperature. For pad thermal expansion, the model uses a simple expansion formula to find the change in thickness. To calculate pad thermal warping, the authors divide the pad into circumferential segments and find the local radius of curvature for each one. This study does not include thermal expansion of the shaft or the bearing housing. To calculate the pad pressure deformation, Wilcock and Booser apply an equivalent bending moment on each circumferential segment. Assuming very small distortions, the pressure deformations accumulate as from an initially flat surface. Finally, the pressure and thermally induced deformations of the pad modify the film thickness. Wilcock and Booser believe that the pad thermal expansion and warping increases the effective preload of the pad. Their results show that accounting for the deformations reduces the mechanical shear power loss, temperature, and eccentricity ratios slightly, but increases the attitude angles. The effect of including deformations on film temperature and minimum film thickness is negligible.

In the same year, Fillon et al. [14] account for the mechanical deformation of the pad and thermally induced deformation of all the bearing components (i.e. pad, shaft, and housing) in a theoretical analysis of TPJBs. The authors study these deformations in the mid-plane of the bearing, neglecting any axial variations. The model uses Finite Element Method to find pad inner surface displacements due to mechanical and thermal loads, and as a constraint, the pivot displacement is set to zero. The model calculates the shaft and housing expansion from a simple formula. For a 4 pad TPJB with journal surface speed of 21 m/s under specific loads up to 1.4 MPa , the authors observe that the pad maximum radial displacement happens at the pivot circumferential location, pressure deformation is only about 10 to 20% of thermally induced deformation, and the expansion of the shaft, pad, and housing reduces the bearing clearance by 25%. Including the deformations also reduces the minimum film thickness on the loaded pads, and substantially decreases the film thickness of unloaded pads. The pressure and thermally induced deformations increase the maximum pressure on all pads about 35%. Fillon et al. observe that neglecting the deformations can cause up to 10 °C discrepancy between pad inner surface temperature predictions and measurements.

In 1991, Brockwell and Dmochowski [15] develop a two dimensional model that accounts for thermal and mechanical deformation effects. In the model, the mean shaft temperature is set equal to sump temperature, and the temperature field in the housing is defined as a hollow

cylinder bounded to the sump oil and ambient air. The authors calculate pad thermal expansion by assuming an average temperature in the radial direction across the pad thickness. A one dimensional beam model that accounts for bending moment, shear forces, and temperature distribution in the pad determines the pad thermal and mechanical distortions. Brockwell and Dmochowski compare the predictions to test data for a 5 pad TPJB with a shaft diameter of 0.076 m operating in LPB configuration, under specific loads between 0.4 MPa and 2.4 MPa. The authors observe that neglecting the radial expansion of the bearing elements (shaft, pad, and housing) over-estimates the eccentricity, and considering them significantly improves the agreement of the predicted eccentricity with measured magnitudes. Brockwell and Dmochowski also find that including the thermal deformations increases the preload in higher loads.

In 2003, He [16] develops a comprehensive two dimensional TEHD model for TPJB analysis that accounts for the pad mechanical and thermal deformations. A two dimensional finite element, in Cartesian coordinates which neglects the pad curvature, determines the pad deformation. A simple thermal expansion formula determines the changes in the shaft and housing radii. The journal temperature can be selected as the average film temperature, an imposed temperature, or resultant temperature from assuming nil net heat flow to the shaft. The housing temperature is set equal to the sump temperature, which is determined from the conservation of energy in the whole bearing, assuming that lubricant absorbs 90% of the mechanical shear power loss. He observes that the temperature maximizes shortly after the minimum film thickness location and subsequently declines. Contrary to pad mechanical deformation, thermally induced deformation of the pad decreases the effective bearing clearance, thus leading to an increase in the pad temperature due to a reduced film thickness. The author concludes that the shaft and housing deformations are important, but lacking accurate thermal boundary conditions, must be approached cautiously.

In 2013, Hagemann et al. [4, 17] present a series of measurements conducted on a large size TPJB (diameter of 0.5 m) subject to a high surface speed (up to 79 m/s) and a heavy load (specific load up to 2.5 MPa), and compare them to the predictions. The prediction model is based on a two-dimensional Reynolds equation and a three-dimensional energy equation for the fluid film and solid elements respectively. The authors note the importance of accurately modeling the oil delivery process, and implement one that establishes an effective supply temperature by accounting for the heat fluxes in the feed groove region. While the authors explain the model, they do not include respective boundary conditions used for the predictions. The computational program is coupled with a commercial structural mechanics software in which the pressure and temperature fields act as boundary conditions to the pad structure to calculate its resultant elastic deformation. A simple formula for one dimensional shaft expansion and pad surface deformation modify the film thickness to determine updated film pressure and

temperature fields. Hagemann et al. account for pad deformation along its axial direction as it is critical to calculating an accurate film thickness. Along the axial plane, the pad warping increases the film thickness at the pad edges relative to the film thickness at the pad mid-plane, thus making an arcuate shape. Similar to an earlier three-dimensional analysis by Desbordes et al. [18], Hagemann et al. [4] conclude that the design, the manufactured size, and the load on the bearing determines the complexity of the analysis. The authors show that for a smaller size bearing (diameter of 0.12 m) operating with similar surface speed and bearing load to the large bearing, the predictions from a simplified model do not have a considerable discrepancy to the sophisticated model. Hagemann et al. argue that using complex and more time consuming model is not indispensable for analysis of a small TPJB (diameter of 0.12 m).

In 2015, Suh and Palazzolo [19] develop a three-dimensional TEHD model for the hydrodynamic fluid film, including the heat conduction and thermally induced elastic deformation in both the shaft and bearing pads. The pad surface deformation and shaft thermal expansion along the radial direction are added to the film thickness formula. In the second part of their work, Suh and Palazzolo [20] compare predictions to selected test data from Kulhanek and Childs [21] for a 5-pad TPJB (rotor diameter of 0.01 m) operating with a surface speed between 37 to 85 m/s, and under a specific load up to 2.4 MPa. The authors note that the bearing stiffness coefficients delivered by the TEHD model are larger than those from EHD models due to a tighter clearance caused by the thermal expansion of both the shaft and pads. Also, the journal eccentricity and average film thickness from the TEHD analysis are lower than corresponding magnitudes from an EHD analysis. Although the pads are hotter than the shaft, the shaft thermal expansion is more than twice the average pad expansion. The authors show that thermal expansion of both the shaft and bearing pads reduces the film thickness, thus increasing the bearing stiffness, even after the reduction in lubricant viscosity due to operation at a hotter temperature. However, the model does not account for the bearing housing expansion. Suh and Palazzolo model predicts higher stiffness coefficients and lower damping coefficient "with 20% maximum error of stiffness coefficients and 30% maximum error of damping coefficient." (although the presented comparisons show larger discrepancies). The authors also analyze three bearing configuration with different pad thicknesses. Their model predicts that both mechanical and thermal deformation act to raise the pad mechanical preload. With a thick pad, the preload increases predominantly due to thermally induced deformations. While with a thin pad, the preload increases primarily due to pressure induced warping. Moreover, the reduction of the damping coefficient for a smaller pad thickness is more pronounced than the reduction of the stiffness coefficient.

In 2013, San Andrés and Tao develop a TPJB analysis program (XLTPJB®) based on thermohydrodynamic bulk flow model for calculation of film temperature and pressure fields. The

model accounts for pivot stiffness, and predicts frequency independent rotordynamic coefficients ($[K,C,M]$ model). Later, San Andrés and Li [2] extend the model to account for pressure induced deformation on each bearing pad. A finite element pad structural model couples to the analysis program that determines the pad deformation due to the hydrodynamic pressure field. The predictions show that including the pad mechanical deformations reduces the predicted stiffness and damping coefficients up to 20%. The authors note that including pivot flexibility for pivots stiffer than the fluid film has only a slight influence on the TPJB force coefficients ($[K,C,M]$). However, for pivots that are substantially more flexible than the fluid film, the bearing stiffness becomes a strong function of the pivot stiffness. Generally, pivot flexibility acts to reduce the damping coefficients more distinctly than the stiffness coefficients.

The scope of this work is to extend the physical model in Refs. [1, 2, 3] to include the thermally induced elastic deformation of the bearing elements (pads, shaft, and housing). Predictions for pad thermally induced deformation add to pressure induced deformation explained in Refs. [2, 3]. Also, expansion of the shaft and the bearing housing changes the pads' operating clearances. Addition of above thermal expansions and pad thermally induced deformation modifies the film thickness and constructs a full TEHD analysis that predicts performance of TPJBs, such as temperatures of bounding solids and fluid film, minimum film thickness, journal eccentricity, and the dynamic force coefficients.

2. ANALYSIS FOR THERMALLY INDUCED PAD ELASTIC DEFORMATIONS

Figure 1 shows the geometry of a tilting pad along with the definition of variables used throughout this section. Here, analytical methods are derived which closely approximate a three-dimensional FEM for thermally induced deformation of a pad. The major assumptions for the derivation are (1) only radial heat transfer occurs through the pad thickness, (2) negligible thermally induced stresses in the pad, (3) superimposed radial deformation calculated separately for the axial and circumferential cross sections. The following explains the governing equations and derivation of pad deformation equation.

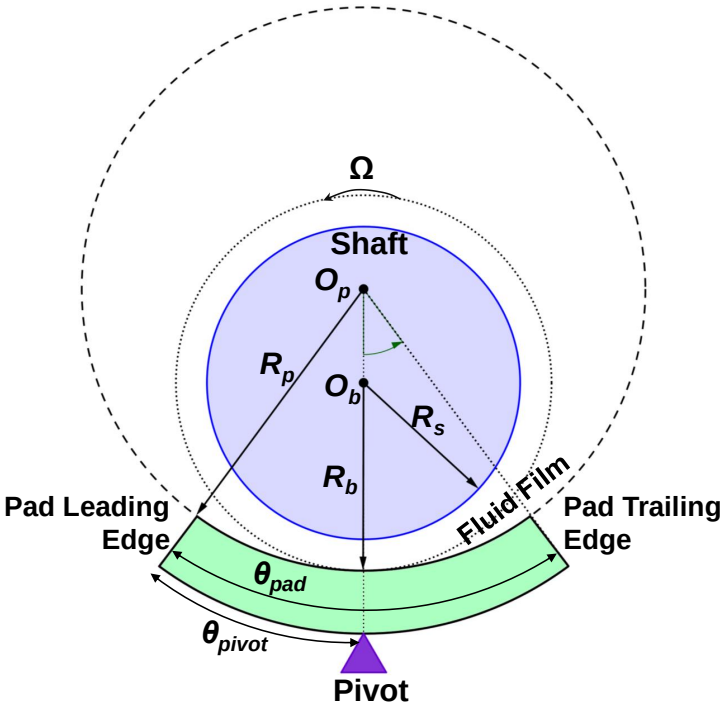

Ω	Shaft rotational speed
O_p	Pad Center
O_b	Bearing Center
R_p	Pad Radius
R_b	Bearing Radius
R_s	Shaft Radius
$C_b = R_b - R_s$	Bearing Clearance
$C_p = R_p - R_s$	Pad Clearance
$m = 1 - C_b/C_p$	Nondimensional Preload
θ_{pivot}	Pivot Arc Angle
θ_{pad}	Pad Arc Angle

Figure 1: Geometry of one tilting pad and nomenclature.

Deformation of bearing components alters the film thickness and influences the bearing static and dynamic load performance. These deformations consist of mechanical deformation due to hydrodynamic pressure and thermally induced deformation due to temperature raise on the pad, shaft, and bearing housing. San Andrés and Li [3] modeled pad mechanical deformation using a three-dimensional finite element structure. The current work extends their model to include thermally induced deformations of a pad in TPJB.

Unlike mechanical deformation produced by the hydrodynamic pressure field on a pad, the thermal deformation depends on the boundary conditions of temperature and heat flow surrounding a pad and that greatly affect the pad ensuing deformed shape. Figure 2 shows the

boundary conditions around a whole pad consisting of fluid film temperature ($T_{(\theta,z)}$) on the pad surface, and the heat flows (Φ) between the pad and the lubricant surrounding it. In addition, shaft and bearing housing temperatures are necessary to determine their thermal expansion along the radial direction.

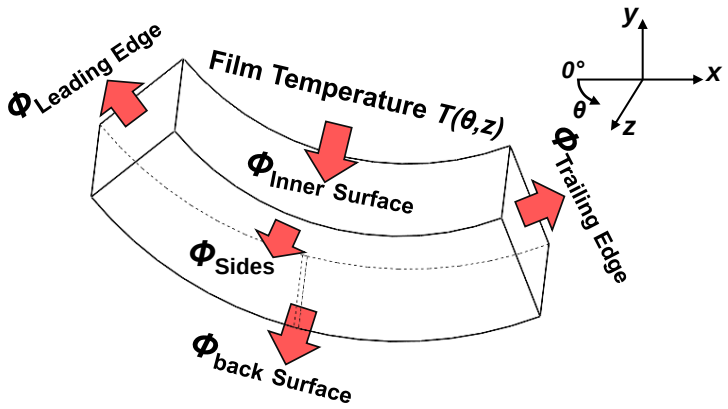

Figure 2: Fluid film temperature on pad surface and heat fluxes (ϕ) on a bearing pad.

Researchers have assumed magnitudes for the heat transfer coefficients on a pad leading edge, trailing edge, sides, and back surface that considerably influence the heat flow to these surfaces while increasing the complexity of a computational model. For example, Wodtke et al. [22] show that for a large size tilting-pad thrust bearing, none of the major assumptions customarily used for the heat convection coefficients provide a satisfactory agreement between a predicted temperature field and test data. These assumed heat convection coefficients vary greatly from 100 W/m^{2}K to 2,840 W/m^{2}K. In short, one cannot expect to increase the accuracy of a physical model by increasing the model complexity while using inadequate boundary conditions.

The following explains briefly the physical model to determine the pressure field in a hydrodynamic film and the temperature field in the fluid film and bounding solids.

2.1. Reynolds Equation

San Andrés and Tao [1] state an extended Reynolds equation governing the generation of the pressure field (p) in a laminar flow TPJB. On a pad, this equation is

$$\frac{1}{R_s^2}\frac{\partial}{\partial\theta}\left(\frac{H^3}{12\mu}\frac{\partial p}{\partial\theta}\right)+\frac{\partial}{\partial z}\left(\frac{H^3}{12\mu}\frac{\partial p}{\partial z}\right)=\frac{\partial H}{\partial t}+\frac{\Omega}{2}\frac{\partial H}{\partial\theta}+\frac{\rho H^2}{12\mu}\frac{\partial^2 H}{\partial t} \tag{1}$$

where the lubricant viscosity (μ) is a function of the temperature field (T), (θ, z) are the circumferential and axial coordinates on the plane of the bearing. The film thickness (H) is

$$H_{(\theta,z)} = \delta_{(\theta,z)} + C_{p,hot} + e_x \cos\theta + e_y \sin\theta + \left[\xi_{pivot} - C_{p,hot} + C_{b,hot}\right]\cos(\theta - \theta_p) + \left[\eta_{pivot} - R_{back}\delta_p\right]\sin(\theta - \theta_p) \quad (2)$$

where e_x, e_y are the journal center displacements, $(\xi_{pivot}, \eta_{pivot})$ are the pad radial and transverse displacements in pad pivot local coordinates. Above, R_{back} is the sum of the pad machined radius and pad thickness at the pivot position, δ_p is the pad tilt angle, and θ_p is the pivot angular position starting from x axis. Above, $C_{p,hot}, C_{b,hot}$ are hot pad clearance and hot bearing clearances defined from cold pad clearance (C_p) and cold bearing clearance (C_b) as,

$$C_{p,hot} = C_p - \Delta R_s + \Delta R_h \text{ and } C_{b,hot} = C_b - \Delta R_s + \Delta R_h \quad (3)$$

The elastic deformation field for each pad ($\delta_{(\theta,z)}$) is added to the film thickness separately. $\delta_{(\theta,z)}$ is along the radial direction and includes both thermally induced and pressure induced deformations.

2.2. BULK FLOW ENERGY TRANSPORT EQUATION

Ref. [23] implements a steady-state bulk flow energy transport equation for a steady state condition and an incompressible fluid. The conservation of energy states that the energy cannot be created or destroyed. Hence, Eq. (4) shows the balance between the energy disposed (LHS) and the energy generated (RHS). The energy is disposed through convection and diffusion in the fluid film, and the generated energy is due to dissipation.

$$C_p\left[\frac{\partial(\rho HUT)}{\partial x} + \frac{\partial(\rho HWT)}{\partial z}\right] + \Phi = H\frac{\Omega R}{2}\frac{\partial p}{\partial x} + \frac{\mu}{H}\left[k_x\left(W^2 + U^2 + \frac{U\Omega R}{2}\right) + k_J\Omega R\left(\frac{\Omega R}{4} - U\right)\right] \quad (4)$$

where C_p is the fluid specific heat, and k_x, k_J are turbulent flow shear parameters, which are local functions of the Reynolds number ($Re = (\rho H\sqrt{U^2+W^2})/\mu$) [23]. TPJBs generally operate in a laminar flow condition; for Re <1000 the shear parameters $k_x = k_J = 12$, and substituting the pressure gradient term Eq. (4) becomes

$$C_p\left[\frac{\partial(\rho HUT)}{\partial x} + \frac{\partial(\rho HWT)}{\partial z}\right] + \Phi = \frac{12\mu}{H}\left(W^2 + U^2 - U\Omega R + \frac{\Omega^2 R^2}{2}\right) \quad (5)$$

where U, W, T are bulk flow (primitive) variables for circumferential speed, axial speed, and temperature, respectively. They express the average magnitudes across the film thickness. Let $\tilde{U}, \tilde{W}, \tilde{T}$ be circumferential speed, axial speed, and temperature with variations across the film thickness, the bulk flow variables are the defined as

$$U = \frac{1}{H}\int_0^H \tilde{U} dy', \; W = \frac{1}{H}\int_0^H \tilde{W} dy', \; T = \frac{1}{H}\int_0^H \tilde{T} dy' \tag{6}$$

Figure 3 shows the journal and a single pad subjected to convection from the fluid film on its inner surface and sump oil on its back surface, and also conduction through its thickness. An analogy between thermal resistance and electrical resistors illustrates the heat transfer coefficients in the bearing.

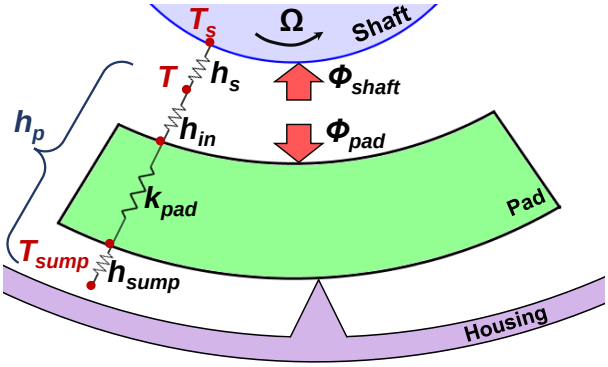

Figure 3: Lumped parameter thermal model accounting for radial conduction and convection to the pad and journal.

In Eqs. (4) and (5), the heat flowing form the film to pad and journal surfaces is

$$\Phi = \underbrace{h_p(T - T_{sump})}_{\Phi_{\text{pad}}} + \underbrace{h_s(T - T_s)}_{\Phi_{\text{shaft}}} \tag{7}$$

where as shown in Figure 3, h_p is the equivalent heat transfer coefficient between the sump region (with temperature T_{sump}) and the film. h_s in the heat transfer coefficient between the film and shaft surface (with temperature T_s).

Following the method implemented by San Andrés and Kim [24] for a lumped parameter thermal model, the equivalent heat convection coefficients for the whole pad (h_p) is regarded as *series* elements,

$$\frac{1}{h_p} = \frac{1}{h_{in}} + \frac{R_{in}}{k_{pad}} \ln\left(\frac{R_{back}}{R_{in}}\right) + \frac{R_{in}}{R_{back} h_{sump}} \tag{8}$$

where k_{pad} is the pad thermal conductivity, and R_{in}, R_{back} are the pad inner surface and

back surface radii, respectively. Above, h_{in}, h_s are determined from an empirical correlation for thermally developing laminar flow (constant wall temperature) by Hausen [25]. Since the flow in the sump region is turbulent due to the oil churning, the heat transfer coefficient for the sump is determined from an empirical correlation for turbulent flow in concentric annular ducts by Gnielinski [26].

Note that this using the empirical correlations generate convection coefficients that are a function of the actual geometry and operating condition of the bearing, such as clearance, shaft diameter, shaft speed, and pad arc length. However, more assumptions still remain (for example the Reynolds number for the sump region). Fortunately, the heat convection coefficients are not very sensitive to the assumed magnitudes in the confines of a typical bearing operation. This method contrasts with the routine practice of assuming a single convection coefficient for the analysis.

2.3. TEMPERATURE DISTRIBUTION IN A PAD

The current model assumes the pad sides are adiabatic (no heat flow, $\Phi = 0$) due to lacking of established heat transfer coefficients for these regions. Hence, in a pad the temperature only varies along the radial direction in a pad, thus allowing for incorporation of the empirical heat convection coefficients. For a film temperature that is only a function of angle ($T_{(\theta)}$), the circumferentially averaged temperature ($\bar{T}_{film}$) is defined as

$$\bar{T}_{film} = \frac{1}{\theta_{pad}} \int T_{(\theta)} \mathrm{d}\theta \tag{9}$$

The differential equation for one-dimensional radial heat conduction in the cylindrical coordinate system

$$\frac{\mathrm{d}}{\mathrm{d}r}\left(r\frac{\mathrm{d}\bar{T}}{\mathrm{d}r}\right) = 0 \tag{10}$$

Integrating for a pad with inner radius of R_{in}, the temperature field ($\bar{T}(r)$) is defined by

$$\bar{T}_{(r)} = a \ln\left(\frac{r}{R_{in}}\right) + b \tag{11}$$

where a, b are the calculated from the heat flux condition at the inner surface and back surface,

namely

$$-K_{pad}\frac{\mathrm{d}\bar{T}}{\mathrm{d}r}\bigg|_{r=R_{in}} = h_{in}\left[\bar{T}_{(R_{in})} - \bar{T}_{film}\right] \tag{12a}$$

$$-K_{pad}\frac{\mathrm{d}\bar{T}}{\mathrm{d}r}\bigg|_{r=R_{back}} = h_{sump}\left[\bar{T}_{(R_{back})} - T_{sump}\right] \tag{12b}$$

Substituting $\bar{T}$ from Eq. (11), Eq. (12) are written as,

$$-K_{pad}\frac{a}{R_{in}} = h_{in}\left[b - \bar{T}_{film}\right] \tag{13a}$$

$$-K_{pad}\frac{a}{R_{back}} = h_{sump}\left[\left(a\ln\left(\frac{R_{back}}{R_{in}}\right) + b\right) - T_{sump}\right] \tag{13b}$$

With simple algebraic manipulations, a, b are expressed as,

$$a = \frac{T_{sump} - \bar{T}_{film}}{\frac{K_{pad}}{R_{in}h_{in}} - \ln\left(\frac{R_{back}}{R_{in}}\right) - \frac{K_{pad}}{R_{back}h_{sump}}} \tag{14a}$$

$$b = \bar{T}_{film} - K_{pad}\frac{a}{R_{in}h_{in}} \tag{14b}$$

Substituting the constants a, b in Eq. (11), the circumferntially averaged temperature distribution across the pad thickness ($\bar{T}_{(r)}$) is determined. The circumferentially averaged temperatures on inner surface and back surface are calculated from $\bar{T}_{in} = \bar{T}_{(R_{in})}$ and $\bar{T}_{back} = \bar{T}_{(R_{back})}$, respectively.

2.4. Lubricant Mixing at a Feed Groove

Figure 4 shows the lubricant supplied into the bearing at a known supply temperature (T_{supply}) and mixed with the hot lubricant leaving the upstream pad with temperature T_i and flow rate Q_i.

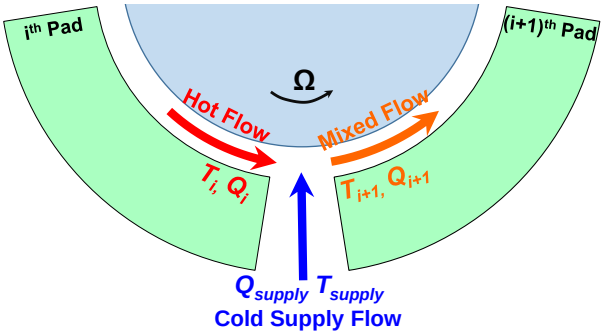

Figure 4: Mixing of hot oil from the upstream pad with cold supply flow in a feed groove region.

A simple *hot* oil mixing model determines the inlet supply flow rate (Q_{supply}) and temperature at the leading edge of the downstream pad (T_{i+1}),

$$Q_{supply} = Q_{i+1} - \lambda Q_i \tag{15a}$$

$$T_{i+1} = \frac{Q_{supply} T_{supply} + \lambda Q_i T_i}{Q_{i+1}} \tag{15b}$$

where λ is a lubricant thermal mixing coefficient. λ is an empirical parameter that depends on the lubrication feed arrangement. The model is simple and does not account for the heat transfer from the pads and oil churning in the groove region. In brief, it is not adequate for some lubricant feeding arrangements. For instance, a single orifice lubricant delivery method ejects the lubricant through the bearing housing, so the cold lubricant mixes with the sump oil before reaching the hot flow from the trailing edge of the upstream pad. On the other hand, a leading edge groove delivers the cold lubricant directly on the leading edge of the pads, minimizing the mixing of supply oil. The model in Eq. (15) is most appropriate for a spray-bar lubrication method.

2.5. PAD THERMALLY INDUCED DEFORMATION

The total strain at each point of a heated body consists of two parts. The first part is a uniform expansion proportional to the temperature rise $\Delta\bar{T} = (\bar{T} - T_{ref})$. This expansion is identical in all directions for an isotropic body, hence only a normal strain and no shearing strain arise. The normal strain in any direction equals to $(\alpha \times \Delta\bar{T})$, with α as the material coefficient of thermal expansion. The second part consists of the strains that maintain the continuity of the body as well as those that arise because of external mechanical loads [27].

A curved beam of constant rectangular cross section models the pad subject to the radial temperature distribution across its thickness. Figure 5 shows the local polar coordinate system defined for a pad. The angle ($\hat{\theta}$) is similar to the angle in bearing cylindrical coordinates (θ), except that it starts from the pivot location on each pad.

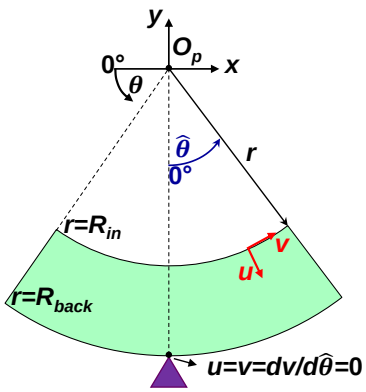

Figure 5: Definition of a pad local coordinate system and deformations (*u, v*) along radial and circumferential directions.

Let u and v be the deformation of a body in the radial and circumferential directions, respectively. Timoshenko and Goodier [28] define the strain components $(\varepsilon_r, \varepsilon_{\hat{\theta}}, \gamma_{r\hat{\theta}})$ in the polar coordinates as,[1]

$$\varepsilon_r = \frac{\partial u}{\partial r} \tag{16a}$$

$$\varepsilon_{\hat{\theta}} = \frac{u}{r} + \frac{\partial v}{r\partial \hat{\theta}} \tag{16b}$$

$$\gamma_{r\hat{\theta}} = \frac{\partial u}{r\partial \hat{\theta}} + \frac{\partial v}{\partial r} - \frac{v}{r} \tag{16c}$$

These expressions for the strain component can be substituted into the generalized equations of Hooke's law for plane stress[2] as,

$$\varepsilon_r = \frac{1}{E}(\sigma_r - \nu\sigma_{\hat{\theta}}) + \alpha\Delta\bar{T} \tag{17a}$$

$$\varepsilon_{\hat{\theta}} = \frac{1}{E}(\sigma_{\hat{\theta}} - \nu\sigma_r) + \alpha\Delta\bar{T} \tag{17b}$$

$$\gamma_{r\hat{\theta}} = \frac{1}{G}\tau_{r\hat{\theta}} \tag{17c}$$

Note that no shearing stress arises due to a change in temperature.

Unlike the strength of materials theory that assumes plane sections must remain plane, the method by Boley and Barrekette [29] calculates the thermal stresses for a one-dimensional temperature distribution $\bar{T}_{(r)}$ using theory of elasticity with no simplifying assumption. The method in Ref. [29] was applied to an arbitrary curved beam with various slenderness ratios (L/D) and temperature boundary conditions. The resultant stresses were compared against

[1] This section follows the general method to find the displacements for symmetrical stress distribution in Ref. [28], page 77.

[2] This method holds for both plane stress and plane strain assumptions since the thermal stresses are neglected.

those from a commercial FE simulation with a similar radial temperature distribution.

It was determined that the magnitude of strain due to the stress terms in Eq. (17) are at least three orders of magnitude[3] smaller than the strains due to thermal expansion term ($\alpha\Delta\bar{T}$). Thus, neglecting the strain terms induced by internal stresses, Eq. (17) reduces to,

$$\varepsilon_r = \alpha\Delta\bar{T} \tag{18a}$$

$$\varepsilon_{\hat{\theta}} = \alpha\Delta\bar{T} \tag{18b}$$

$$\gamma_{r\hat{\theta}} = 0 \tag{18c}$$

where the circumferentially average temperature rise ($\Delta\bar{T}$) is the temperature rise from a reference 'cold' temperature (T_{ref}) along the radial direction across the pad.

$$\Delta\bar{T} = \bar{T}_{(r)} - T_{ref} = a\ln(r/R_{in}) + \underbrace{\left[b - T_{ref}\right]}_{b'} \tag{19}$$

Above, a and b are constants determined from the heat convection boundary condition, defined in Eq. (14). Substituting the radial and circumferential strains from Eq. (18) into Eq. (16) and integrating yields,

$$u_{(r,\hat{\theta})} = \int \varepsilon_r \mathrm{d}r + f_{1_{(\hat{\theta})}} = \alpha r\left(a\ln\left(\frac{r}{R_{in}}\right) - a + b'\right) + f_{1_{(\hat{\theta})}} \tag{20a}$$

$$v_{(r,\hat{\theta})} = \int (r\varepsilon_{\hat{\theta}} - u)\mathrm{d}\hat{\theta} + f_{2_{(r)}} = \alpha a r\hat{\theta} - \int f_{1_{(\hat{\theta})}}\mathrm{d}\hat{\theta} + f_{2_{(r)}} \tag{20b}$$

in which $f_{1_{(\hat{\theta})}}$ is a function of $\hat{\theta}$ only, and $f_{2_{(r)}}$ is a function of r only. Substituting Eq. (20) into Eq. (16c) and noting that $\gamma_{r\hat{\theta}}$ is nil, then,

$$\frac{\mathrm{d}f_{2_{(r)}}}{\mathrm{d}r} - \frac{1}{r}f_{2_{(r)}} = -\frac{1}{r}\frac{\mathrm{d}f_{1_{(\hat{\theta})}}}{\mathrm{d}\hat{\theta}} - \frac{1}{r}\int f_{1_{(\hat{\theta})}}\mathrm{d}\hat{\theta} \tag{21}$$

The above equation can only be obtained for symmetrical stresses[4]. For a non-symmetric stress distribution (i.e. a point load at one end) terms that are function of both r and $\hat{\theta}$ would not cancel out and the following method, namely separation of variables, cannot be used. In the current method, as explained in Appendix A, the stresses are taken as zero, hence symmetric.

[3] Appendix A provides the formulation of the thermal stresses and a numerical example.

[4] Both σ_r and σ_θ must be independent of θ, and only a function of r.

Since $f_{1_{(\hat{\theta})}}$ and $f_{2_{(r)}}$ are respectively functions of r and $\hat{\theta}$ only, Eq. (21) is written as,

$$\frac{\mathrm{d}f_{2_{(r)}}}{\mathrm{d}r} - \frac{1}{r} f_{2_{(r)}} = A_0 \tag{22a}$$

$$-\frac{1}{r}\frac{\mathrm{d}f_{1_{(\hat{\theta})}}}{\mathrm{d}\hat{\theta}} - \frac{1}{r}\int f_{1_{(\hat{\theta})}}\mathrm{d}\hat{\theta} = A_0 \tag{22b}$$

Solving the ordinary differential equations above yields,

$$f_{2_{(r)}} = A_0\,(\ln r + A_1)\,r \tag{23a}$$

$$f_{1_{(\hat{\theta})}} = A_0 + A_2 \sin\hat{\theta} + A_3 \cos\hat{\theta} \tag{23b}$$

where the end conditions of the curved beam determine the constants $A_0, A_1, A_2,$ and A_3. By representing the pivot as a fixed point, one can use a local polar coordinate for each pad with $\hat{\theta} = 0$ at the pivot. Thus, the boundary conditions become

$$\text{at the pivot } \hat{\theta} = 0 \text{ and } r = R_{back}\text{: } u = v = \frac{\partial v}{\partial r} = 0 \text{ (no deformation)}$$

Applying these boundary conditions to Eq. (20), the constants become

$$A_3 = \alpha R_{back}\left[a\ln\left(\frac{R_{back}}{R_{in}}\right) - a + b'\right], \text{and } A_0 = A_1 = A_2 = 0$$

Hence, the radial and circumferential displacements (u, v) of a pad are

$$u_{(r,\hat{\theta})} = -\alpha\left[aR_{back}\ln\left(\frac{R_{back}}{R_{in}}\right)\cos\hat{\theta} - ar\ln\left(\frac{r}{R_{in}}\right) + (r - R_{back}\cos\hat{\theta})(a - b')\right] \tag{24a}$$

$$v_{(r,\hat{\theta})} = \alpha\left[aR_{back}\ln\left(\frac{R_{back}}{R_{in}}\right)\sin\hat{\theta} - R_{back}(a - b')\sin\hat{\theta} + ar\hat{\theta}\right] \tag{24b}$$

where a and b' are constants specified from the thermal boundary conditions as

$$a = \frac{T_{sump} - \bar{T}_{film}}{\frac{K_{pad}}{R_{in}h_{in}} - \ln\left(\frac{R_{back}}{R_{in}}\right) - \frac{K_{pad}}{R_{back}h_{sump}}}$$

$$b' = \bar{T}_{film} - K_{pad}\frac{a}{R_{in}h_{in}} - T_{ref}$$

Recall, the radial deformation of the inner surface at the mid-plane is $u_{(R_{in},\hat{\theta})}$.

Figure 6 shows a schematic view of the deformation of pad along the pad length (axial direction). Existing analyses customarily neglect pad thermal warping along the axial direction

in a two dimensional deformation analysis. The following explains an approximate method to account for the axial deformation of a pad.

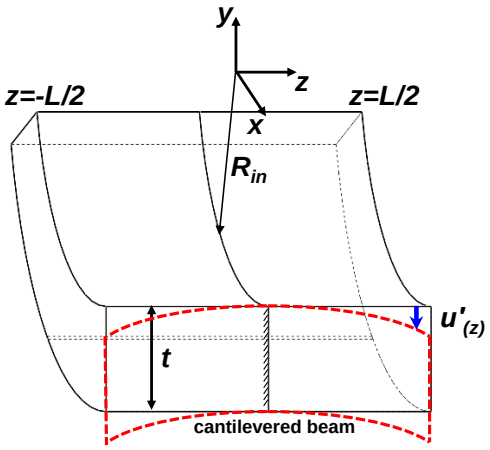

Figure 6: Definition of an assumed cantilevered beam to approximate pad warping along the axial direction.

A pad does not have a curvature along the axial (z) direction, so it is modeled by an Euler beam, cantilevered at the mid plane, subjected to the stated temperature boundary condition ($\bar{T}_{in}, \bar{T}_{back}$). The reference temperature is equal to the pad average temperature ($T_{ref} = (\bar{T}_{in} + \bar{T}_{back})/2$) since the expansion of the pad is already considered for the mid-plane deformation via Eq. (24). Thus, the thermal deformations only produce bending in the axial direction. The assumed beam length is 50% of the pad length ($L/2$).

Using the general method in Ref. [30], the axial thermal warping as a function of axial distance (z) to the mid-plane becomes,

$$u'_{(z)} = \alpha \frac{\bar{T}_{in} - \bar{T}_{back}}{2t} z^2 \quad \text{for} \quad \frac{-L}{2} < z < \frac{L}{2} \tag{25}$$

Finally, the deflection of the inner surface of the pad ($\delta_{(\hat{\theta},z)}$) along the radial direction is defined as the superposition of deformation in the circumferential and axial cross sections,

$$\delta_{(\hat{\theta},z)} = u_{(R_{in},\hat{\theta})} + u'_{(z)} \tag{26}$$

Figure 7 shows the radial deformation of pad inner surface from this method in comparison with the full results from a three-dimensional structural FE pad model. The geometry of the pad is taken from Coghlan, Ref. [5]. The inner radius of the pad (R_{in}) is 0.051 m, the outer radius (R_{back}) is 0.07 m, and the pad axial length (L) is 0.061 m. The pad material thermal expansion coefficient (α) is 1.3×10^{-5} 1/°C, and the temperature boundary conditions for the inner and back surfaces are respectively $\bar{T}_{in} = 80°\text{C}, \bar{T}_{back} = 72°\text{C}$. The reference temperature

is $T_{ref} = 21°\text{C}$. One can observe that the results from the analytical model approximates the three dimensional deformation field closely.

However, note that the FEM results are for a pad with a radial temperature distribution, and the deformation due to three-dimensional temperature distribution in the pad might differ slightly.

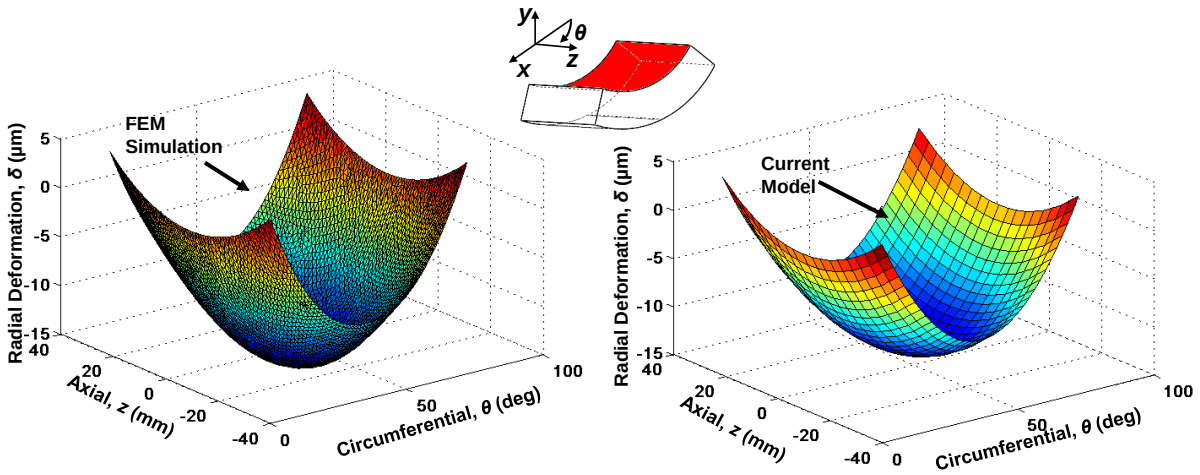

Figure 7: Pad inner surface thermally induced deformation. Comparison of results from the current analytical method (right) versus 3D FEM (right). Reference geometry taken from Ref. [7]

2.6. SHAFT EXPANSION AND HOUSING EXPANSION

Accurate modeling of the journal thermally induced deformation requires the solution of the temperature field for the entire shaft. Similarly, the bearing housing installation type and the operating conditions determine the temperature field in the bearing housing. Therefore, the thermal expansion of shaft OD and housing ID is modeled using a simple one-dimensional formula, i.e.,

$$\Delta R_s = \alpha_s R_s (T_s - T_{ref}) \tag{27a}$$

$$\Delta R_h = \alpha_h R_h (T_h - T_{ref}) \tag{27b}$$

where α_s and α_h are the shaft and housing material thermal expansion coefficient. Above, the subscripts s and h denote shaft OD and housing ID, respectively.

The shaft temperature is either imposed or calculated as the average of film temperature throughout the bearing. The temperature measurements from Coghlan [5] show that the housing temperature is very close to the oil discharge temperature. Presently, the model takes the sump (discharge) temperature as the housing temperature (T_{sump}).

Contrary to the shaft that only expands outward, the housing expansion or contraction is

dependent on its installation condition. If the housing is free (such as in some test rigs), it expands outward. Alas for most practical cases, the housing contracts as it is firmly affixed or press inserted into a pedestal, for example.

2.7. HOT CLEARANCE ESTIMATION

A geometric model estimates the change in the pad clearance and bearing clearance due to both mechanical and/or thermally induced deformations. After the calculation of pad deformations a new origin (O'_p) is found for the deformed pad. New pad clearance is based on new pad radius (R'_p) and expansion of the shaft and bearing housing.

Figure 8 (left) shows the circumcenter of a triangle[5] on a pad inner surface formed by the leading edge, pivot location, and trailing edge points. Each side of this triangle is a chord of the circumcircle. Figure 8 (right) shows the thermally induced deformed shape of a pad. The model finds the midpoint of the line segments that connect the trailing edge and leading edge to the pivot. Then it determines the slopes of these segments, and the slopes of their perpendicular bisectors. This gives enough information to state the geometric relation of the two perpendicular bisectors. The intersection of these lines is the deformed pad arc center, and the new pad radius (R'_p) is calculated with respect to this point.

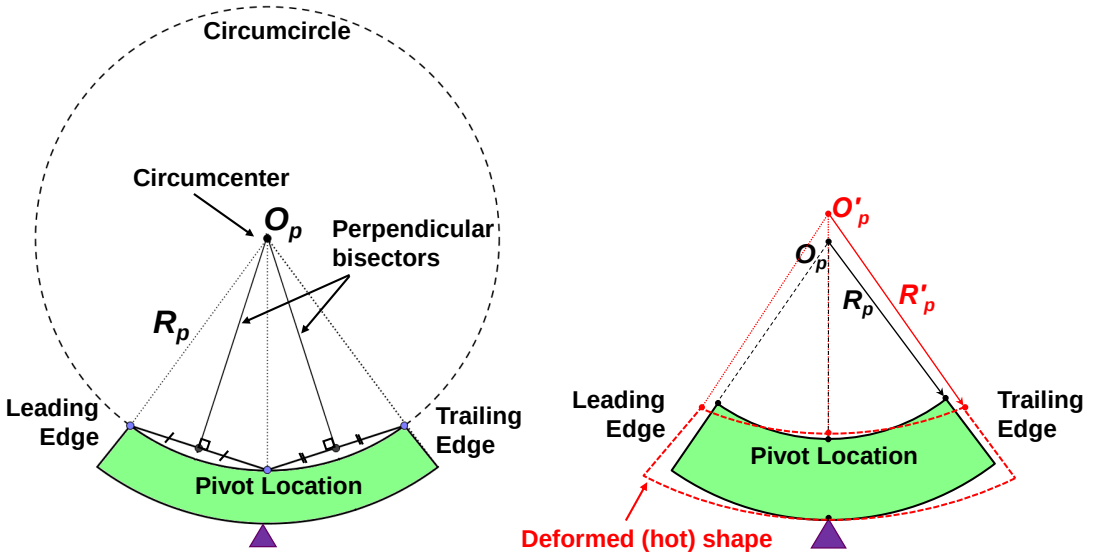

Figure 8: *Left:* Circumcenter of a pad, *Right:* Thermal deformation of a pad, includes the effects of thermal expansion and warping.

The new bearing radius (R'_b) is the difference between the deformed pivot location on the

[5]The point at which the perpendicular bisectors of the sides of a triangle intersect and which is equidistant from the three vertices. The perpendicular bisector of a segment is a line that is perpendicular to the segment, and intersects with the midpoint of the segment.

inner surface and the bearing origin. New pad and bearing clearances with the contributions of the pad, shaft, and housing deformations are

$$C'_p = R'_p - R_s - \Delta R_s + \Delta R_h \tag{28a}$$

$$C'_b = R'_b - R_s - \Delta R_s + \Delta R_h \tag{28b}$$

Thus the new preload becomes,

$$m' = \frac{C'_p - C'_b}{C'_p} = \frac{R'_p - R'_b}{R'_p - R_s - \Delta R_s + \Delta R_h} \tag{29}$$

Note that the pad clearances calculated from this method are larger than the actual deformed shape clearance because of the assumption that deformed pad inner surface remains circular. To calculate the film thickness (Eq. (2)) the deformation field of the pad surface ($\delta_{(\hat{\theta},z)}$) and changes in shaft and housing radius ($\Delta R_s, \Delta R_h$) are used separately.

3. COMPARISON OF PREDICTIONS AGAINST TEST DATA

3.1. LARGE SIZE TPJB UNDER HIGH SURFACE SPEED AND HEAVY LOAD

Table 1 outlines the geometry, lubricant properties, and operating conditions of a large size test bearing. Figure 9 shows a schematic view of the bearing and the load direction. The measurements and predictions from the computational model in Ref. [4, 17] are compared against the predictions obtained using the current model.

Table 1: Characteristics of a TPJB tested by Hagemann et al. [4]

Bearing properties	
Load orientation	LBP
Number of pads	5
Shaft diameter [mm]	500
Pad thickness [mm]	72.5
Bearing axial length [mm]	350
Pad arc length	56°
Pivot offset	0.6
Pad clearance [μm]	300
Preload	0.23
Pad mass* [kg]	55.9
Pad moment of inertia about pivot point* [kg·m^2]	0.44
Pivot Stiffness* [N/m]	5×10^9
Operating condition	
Load [kN]	175–438
Specific Load $W/(LD)$ [MPa]	1–2.5
Shaft rotational speed [RPM]	500–3000
Shaft surface speed ΩR [m/s]	13–79
Lubricant supply temperature [°C]	50
Lubricant flow rate [LPM]	210 / 420
Fluid properties	
Lubricant	ISO VG32
Viscosity at supply temperature* [mPa·s]	22.4
Viscosity temperature coefficient* [1/°C]	0.0297
Density [kg/m^3]	844
Specific heat capacity [kJ/(kg·K)]	2.17
Thermal conductivity [W/(m·K)]	0.13
Lubricant supply method	Spray-bar
Thermal properties	
Pad and journal thermal conductivity [W/(m·K)]	45
Sump temperature [°C]	65
Housing direction of expansion*	Outwards
Thermal mixing coefficient λ*	0.8 (3 kRPM) 0.5 (1.5 kRPM)

*Assumed or calculated based on the available data.

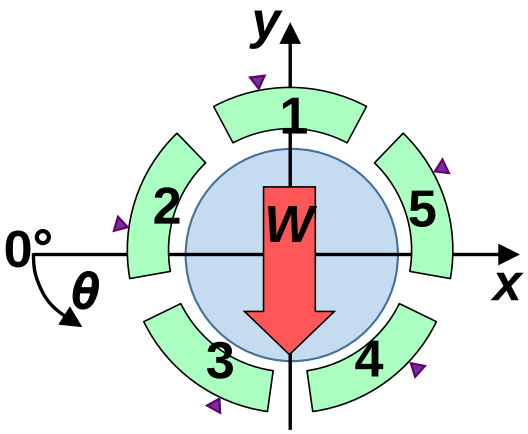

Figure 9: Schematic view of a five-pad TPJB in Ref. [4].

Hagemann et al. [4] use a test rig designed for large size turbine bearings with a diameter of 500 mm and maximum length of 500 mm. The driving power (1.2 MW) enables a operating shaft speed up to 4000 RPM. The authors equip the hollow shaft with two piezoelectric pressure sensors and two capacitive displacement sensors. Subsequently, the test procedure shifts the shaft axially during the measurement with a speed of 500 mm/min, which enables capturing the whole film thickness and pressure distribution with a high resolution. Hagemann et al. determine the dynamic force coefficients of the test bearing from relative displacement between shaft and bearing.

The maximum applied load on this bearing (by pulling the test bearing) is 1 MN. Yet, due to the large size of the bearing, the specific load is between 1 MPa and 2.5 MPa. Also, the large diameter of the rotor gives a high surface speed (between 13 m/s and 79 m/s) for shaft speeds between 500 RPM and 3,000 RPM. For this test bearing, the length to diameter (L/D)=0.7 and clearance to radius ratio (C_p/R_s)=0.0012. Rocker pivots, with an arch in the axial direction, enable the pads to tilt in the axial and circumferential directions. Based on the descriptions in Ref. [17], the pivot stiffness is taken as 5×10^9 N/m.

The computational model in Ref. [4] is based on a two-dimensional Reynolds equation and a three-dimensional energy equation for the fluid film and solid elements coupled with a commercial structural software that calculates the mechanical and thermal deformations of the pad.

Table 2 compares the journal eccentricity along the load direction (e_y) obtained for the TEHD and THD predictions. Predicted journal eccentricity in orthogonal direction (e_x) and the journal attitude angle ($\phi = \tan^{-1}(e_x/e_y)$) are very small and not shown. Hagemann et al. [4] do not report these magnitudes. Predicted journal eccentricity from TEHD analysis is smaller in the load direction compared to the predictions from THD analysis. The maximum difference between TEHD and THD prediction is 13% for $W/(LD)$=1 MPa.

Table 2: TEHD and THD predictions for journal eccentricity in the load direction (e_y) for various specific loads. (*N*=3000 RPM)

	$W/(LD)$ [MPa]	1	1.5	2	2.5
THD	e_y [μm]	-125.6	-169.6	-202.3	-231.0
TEHD	e_y [μm]	-111.0	-155.1	-187.9	-218.3

Figure 10 shows[6] the hydrodynamic pressure in the mid-plane of the bearing. The TEHD analysis, including thermal and mechanical deformations, shows very good agreement with the measurements in Ref. [4]. However, observe that not including the thermally induced deformation leads to under-predicting the pressure, in particular its peak magnitude. Note the peak pressure TEHD prediction is 8%[7] larger than the measured magnitude, whereas the THD prediction is 22% smaller. Observe that the pad pressure has a substantial discrepancy with the test data for the lighter loaded pads (1, 2, 5). The TEHD predictions are only slightly improved from the THD predictions.

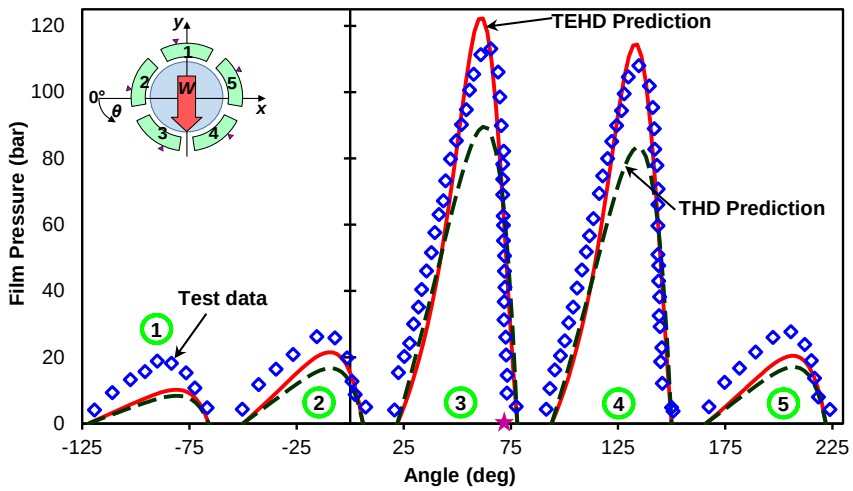

Figure 10: TEHD and THD predictions for mid-plane film pressure compared against test data from Ref. [4]. Star symbol (★) shows the location of minimum film thickness. (*N*=3000 RPM, *W/(LD)*=2.5 MPa)

Figure 11 shows the temperature rise relative to the supply temperature (50°C) on the inner surface of the pads operating with a journal speed of 3,000 RPM and under a specific load of 2.5 MPa. The measured pad temperatures are recorded using thermocouples located 5 mm behind the pad inner surface [4]. The predictions show the film temperature.

[6] In the following figures, 'TEHD' denotes thermoelastohydrodynamic, and 'THD' notation represents thermo-hydrodynamic analysis, that neglects both the thermally and mechanically induced deformation in the bearing components.

[7] The percentage of prediction error compared to measured magnitudes throughout this work is calculated from: %Error=(Measured-Predicted)/Measured.

The predicted temperatures are in good agreement with the measured ones for the highest loaded pads (3, 4). Accounting for both pressure and temperature induced elastic deformations of the pad improves the agreement between the temperature predictions and the test data. The maximum temperature (on pad 3) from the THD analysis is 8.6°C lower than the corresponding temperature, in a TEHD analysis.

On the other hand, film temperature for the lighter loaded pads (1, 2, 5) shows substantial discrepancy with the test data. For the highest loaded pads (3, 4) the maximum difference between the TEHD predictions and the measurements for pad inner surface temperature is 5%, while for the lighter loaded pads (1, 2, 5) the maximum difference is about 70%.

The prediction model finds the temperature field assuming that all of the pads are fully lubricated. Hagemann et al. [4] state that the inlet flow rate during the test was reduced by sealing baffles which influence a flooded lubrication. The predicted lubricant flow rate (658 LPM) is 56% higher than the test condition (420 LPM), which suggests that the lighter loaded pads (1, 2, 5) are not fully wetted. Hence, the higher flow rate on the lighter loaded pads (1, 2, 5) is responsible for the discrepancy between predictions and test data.

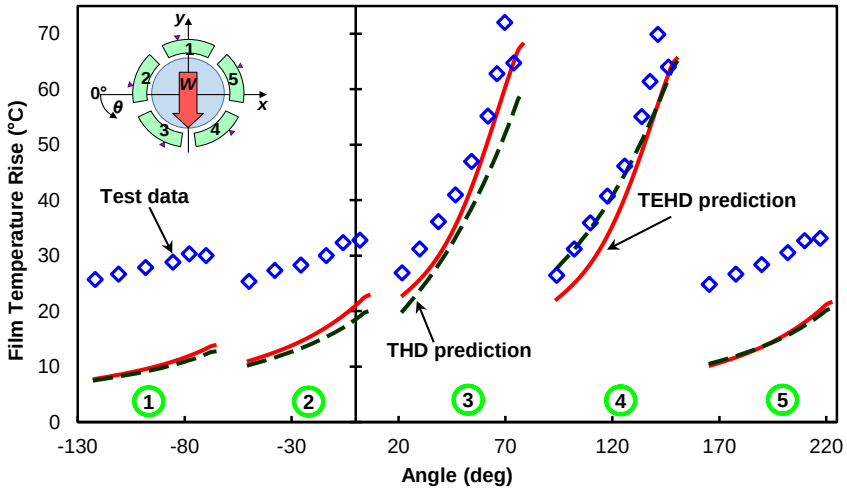

Figure 11: Predicted and measured film temperature rise relative to supply temperature (50°C). TEHD and THD predictions compared against test data from Ref. [4]. (*N*=3000 RPM, *W/(LD)*=2.5 MPa, and λ=0.8)

Figure 12 shows the predicted thermal and pressure deformations on the bearing pads. The total deformation adds to the film thickness, and modifies the performance of the TPJB. Observe that the thermal deformations are generally negative, which means the pads expand toward the center of the bearing. However, the thermally induced deformation is either positive or negative with a smaller absolute magnitude at the leading edge and trailing edge (due to the thermal warping of the pad). For a typical pad, the thermal expansion and warping are closely

related to the pad thickness and arc length. Thicker and shorter pads tend to expand more while slender and longer pads predominantly warp under a given thermal gradient.

In Figure 12, mechanical deformations are always positive due to the opening up of the pad curvature under the pressure. For the highest loaded pads (3, 4) the total deformation is considerable, the maximum deformation is slightly more than the 20% of the cold pad clearance ($C_p = 300$ µm). Pivot offset (0.6) causes an asymmetry in the deformations, with their minimum at the pivot location.

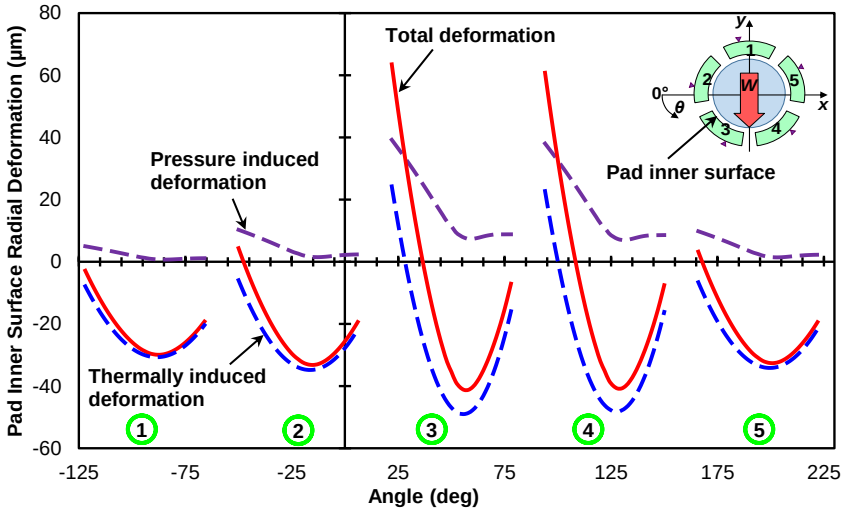

Figure 12: Predicted pads' inner surface deformation along the radial direction. Positive denotes (outward) expansion, while negative magnitude denotes (inward) contraction. (*N*=3000 RPM, *W/(LD)*=2.5 MPa)

Figure 13 shows the film thickness at the mid-plane of the bearing. The TEHD predictions, which include the pressure and thermally induced elastic deformations, generally deliver a lower film thickness compared to that from the THD model. In addition, TEHD predictions have a better agreement with test data for the minimum film thickness. On pad 3, the minimum film thickness in the TEHD prediction is 18 µm larger than the measured magnitude, while for the THD prediction it is 34 µm larger. Relative to minim film thickness, the TEHD model improves agreement of the THD predictions to test data by 56%. However, compared to maximum film thickness these differences are under 5%. In addition, the THD analysis considerably under-predicts the film thickness at the leading edge of the highest loaded pads (3, 4). This is directly due to the pressure deformation (opening up) of these pads due to the applied load.

Note the predicted minimum film thicknesses on pad 1 and 5 are larger than the measured magnitudes. As mentioned above, this phenomena is due to the fact that the test bearing was operating under a starved condition, but the current model predicts the performance of a flooded bearing.

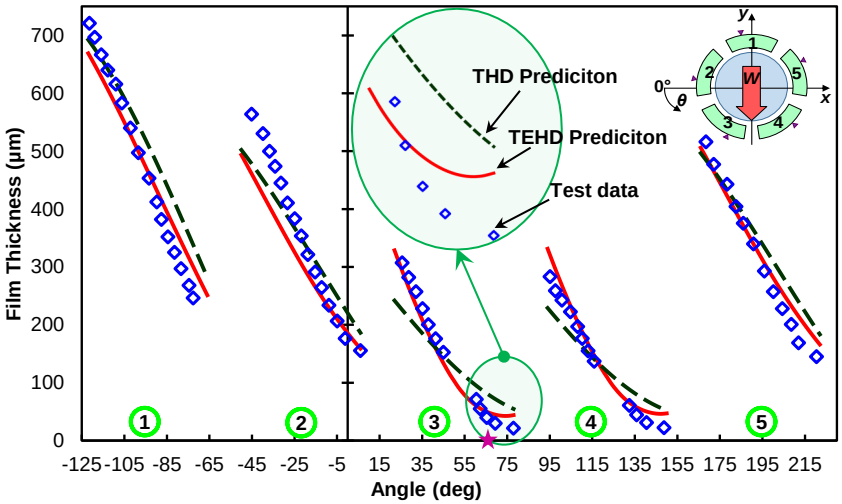

Figure 13: TEHD and THD predictions for mid-plane film thickness compared against test data from Ref. [4]. Star symbol (★) shows the location of peak pressure. (*N*=3000 RPM, *W/(LD)*=2.5 MPa)

Figure 14 shows the axial variation of the film pressure at the circumferential location of peak pressure on the most loaded pad (3). Including the thermally induced deformation causes a considerable increase in peak pressure, and a better agreement with test data. The peak pressure develops shortly before the minimum film thickness, at $\theta = 62°$ on pad 3 (see ★ in Figure 10)

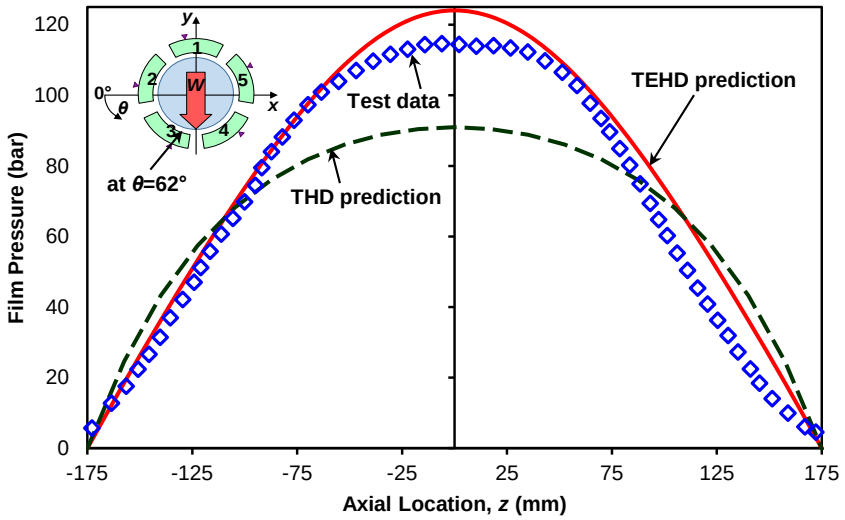

Figure 14: Predicted and measured film pressure at the circumferential location of peak pressure (*θ*=62°, see Figure 10). TEHD and THD predictions compared against test data from Ref. [4]. (*N*=3000 RPM, *W/(LD)*=2.5)

Figure 15 shows the axial variation of the film at its minimum thickness location, shortly downstream of the peak pressure location (θ=74°, see ★ in Figure 13). While prior research typically neglects the axial deformation of a pad, the test data show that this deformation is

significant. The one-dimensional cantilever beam in the current method approximates well the axial deformation. The TEHD predictions for film thickness at z =-½L, 0 , ½L are about 8, 20, 17 μm lower than the measured magnitudes. When compared to the cold pad clearance (300 μm), these differences are very small.

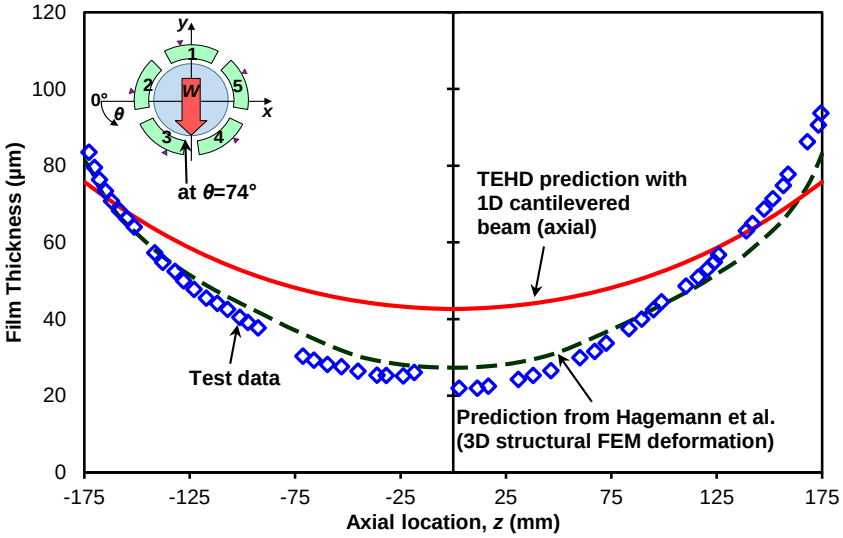

Figure 15: Predicted and measured film thickness in the circumferential location of the minimum film thickness (*θ*=74°, see Figure 13). Measured results from Ref. [4]. (*N*=3000 RPM, *W/(LD)*=2.5 MPa)

Figure 16 shows the predicted (TEHD) direct stiffness coefficients for the test bearing compared to the measurements and predictions in Ref. [17]. Kukla et al. [17] use the $[K,C]$ model to describe the dynamic coefficients of the TPJB, thus the predictions shown are reduced synchronous with speed. Predicted cross-coupled stiffnesses from the current model are much smaller compared to the measured magnitudes and not shown. The direct stiffnesses (K_{xx}, K_{yy}) depend on the applied load; and for a given shaft speed they increase with an increase in load. Note the pivot stiffness (5000 MN/m) us of the same order of magnitude as the bearing direct stiffness coefficients.

The current predictions and those from Ref. [17] are greater than the measured coefficients. The predicted stiffnesses for $N = 3{,}000$ RPM are slightly larger than the predicted ones for $N = 1{,}500$ RPM; however, the test data show that stiffnesses reduce substantially for $N = 3{,}000$ RPM compared to $N = 1{,}500$ RPM. The prediction and measurements show $K_{yy} > K_{xx}$. This stiffness orthotropy in the test data increases when rotor speed increases from $N = 1{,}500$ to $3{,}000$ RPM. This is not reflected by the predictions. The current model and Ref. [17] predict that the direct stiffness orthotropy reduces for the high shaft speed (3,000 RPM).

The agreement of the current TEHD predictions and the test data in the load direction (K_{yy}) is better; for $N = 1{,}500$ RPM, the difference is between 12% and 38%, while in the orthogonal

direction (K_{xx}) the difference is between 29% and 60%. For the high speed ($N = 3{,}000$ RPM), the difference between prediction and test data (K_{yy}) is between 20% and 34%, and for (K_{xx}) it is between 113% and 154%. The predictions in Ref. [17] have a substantially larger discrepancy with the test data for the high speed (3,000 RPM).

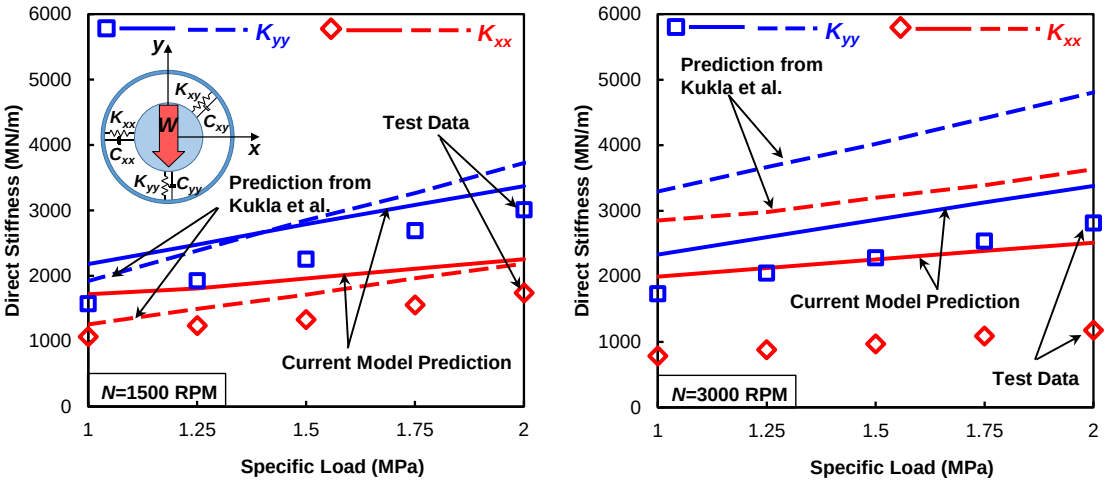

Figure 16: Direct stiffness coefficients (K_{yy}, K_{xx}) versus specific load for operation at two shaft speeds. TEHD prediction and test data from Ref. [17]. (Synchronous excitation; *Left: N*=1500 RPM, λ=0.5; *Right: N*=3000 RPM, λ=0.8)

Figure 17 shows the predicted direct damping coefficients (C_{xx}, C_{yy}) compared to the measurements and predictions in Ref. [17]. The predictions and measurements show $C_{yy} > C_{xx}$. Predicted cross coupled terms are much smaller than the test data and not shown. The predicted direct damping coefficients are consistently smaller than the measurements. Contrary to the measurements and prediction in Ref. [17], the current model predicts that the damping coefficients decrease with an increase in load.

The agreement of the current prediction and test data in the load direction (C_{yy}) is better; for $N = 1500$ RPM the difference is between 1% and 16%, while in orthogonal direction (C_{xx}) the difference is between 1% and 23%. The predictions in Ref. [17] have a substantially larger discrepancy for the low speed (1500 RPM). For the high speed ($N = 3000$ RPM), the difference between prediction and test data for C_{yy} is between 35% and 49%, and for C_{xx} it is between 33% and 41%.

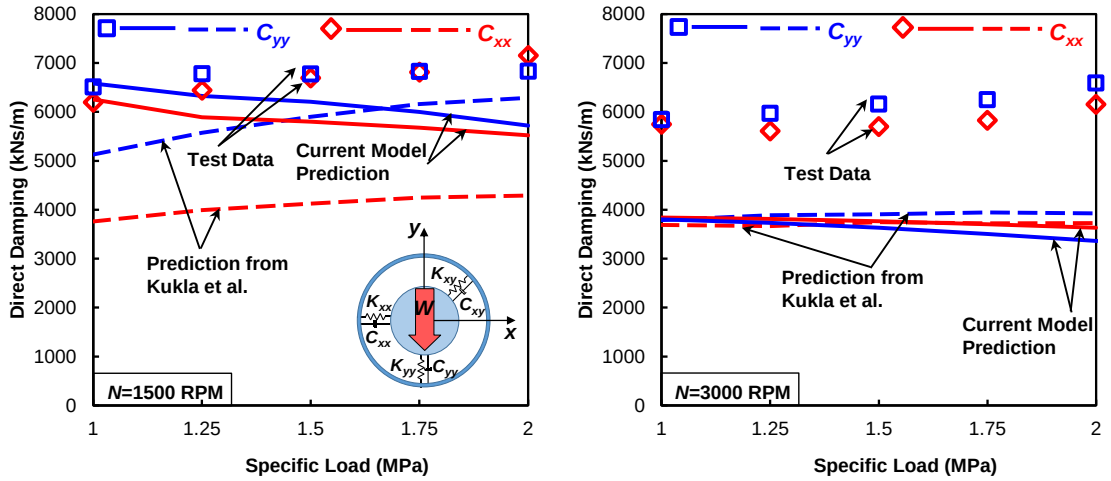

Figure 17: Direct damping coefficients (C_{yy}, C_{xx}) for operation at two shaft speeds. Prediction and test data from Ref. [17]. (Synchronous excitation; *Left:* N=1500 RPM, λ=0.5; *Right:* N=3000 RPM, λ=0.8)

The results above (Figures 16 and 17) are of interest due to the large deviation between the predictions and the test results. Kukla et al. [17] believe that no fundamental error occurred in the analysis or test procedure. The authors state the key problem of the test procedure,

"The dynamic force component is gathered from the fluid film while the force itself is applied externally. Thus, it is assumed that the bearing force is equal to the fluid force in every time step. This is only correct if pad inertia effects have no significant influence on the pad movement." Kukla et al. also believe that neglecting the axial shifting of the shaft in the support bearings, and its dynamic behavior might have been responsible for the discrepancies.

Based on the available geometry in Ref. [17], the pad mass and moment of inertia are calculated as 55.9 kg and 0.44 kg·m^2, respectively. The virtual mass term in $[K,C,M]$ prediction model is very large and reduces the stiffness coefficients. The predicted damping coefficients do not noticeably differ in the $[K,C,M]$ and $[K,C]$ model. These results, however, cannot be compared with the test data in Ref. [17] since Kukla et al. used a $[K,C]$ model for the test data.

3.2. SPHERICAL SEAT TPJB UNDER HEAVY SPECIFIC LOAD AND HIGH SPEED

Recently, Coghlan and Childs [5, 6] conducted an extensive test program to study the effects of various lubrication (oil feed) configurations on the static and dynamic force performance of a spherical seat TPJB. Table 3 shows the characteristics of the test bearing in Ref. [5] and Figure 18 shows a schematic view of the bearing and the load direction.

Table 3: Characteristics of a TPJB tested by Coghlan and Childs [5]

Bearing properties	
Load orientation	LBP
Number of pads	4
Shaft diameter [mm]	101.59
Pad thickness [mm]	190
Bearing axial length [mm]	61
Pad arc length	72°
Pivot offset	0.5
Pad clearance [μm]	134
Preload	0.3
Pad mass* [kg]	0.6
Pad moment of inertia about pivot point* [kg·m^2]	4.6×10^{-4}
Pivot Stiffness [N/m]	4.12×10^{8}
Operating condition	
Load [kN]	4.3 - 17.7
Specific Load $W/(LD)$ [MPa]	0.7–2.9
Shaft rotational speed [RPM]	7000–16000
Shaft surface speed ΩR [m/s]	38–85
Lubricant supply temperature [°C]	48.9
Lubricant flow rate [LPM]	38 (flooded) / 42 (evacuated)
Fluid properties	
Lubricant	ISO VG46
Viscosity at supply temperature [mPa·s]	25.6
Viscosity temperature coefficient	0.0431 1/°C
Density [kg/m^3]	843.5
Specific heat capacity [kJ/(kg·K)]	2.084
Thermal conductivity [W/(m·K)]	0.1243
Thermal properties	
Pad and journal thermal conductivity [W/(m·K)]	52
Sump temperature [°C]	51–64
Housing direction of expansion*	Outwards
Shaft thermal expansion coefficient [1/°C]	1.23×10^{-5}
Pad thermal expansion coefficient [1/°C]	1.30×10^{-5}
Thermal mixing coefficient λ*	0.5 (7 kRPM), 0.6 (10 kRPM) 0.7 (13 kRPM), 0.8 (16 kRPM)

*Assumed based on the available data.

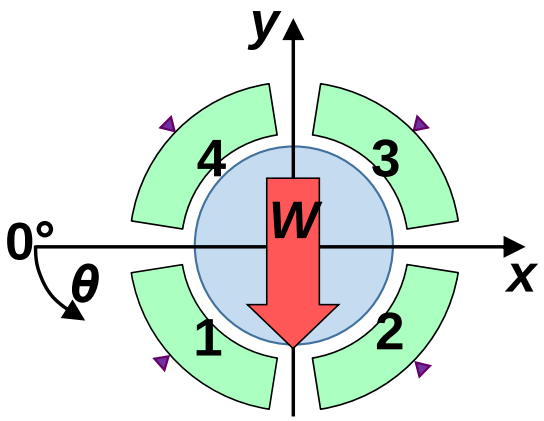

Figure 18: Schematic view of the four-pad TPJB in Ref. [5]

The test bearing is measured various lubrication delivery methods,

1. Flooded single-orifice (SO)
2. Evacuated leading edge groove (LEG)
3. Evacuated spray-bar (SB)
4. Evacuated spray-bar blocker (SBB)

The authors compare their test results with THD predictions obtained from XLTPJB® [1], including the pivot deformation. However, their predictions do not account for the mechanical and thermal elastic deformations (only approximation of *hot* clearances).

The predictions of the current model are compared to the test results in Ref. [5] for an evacuated spray-bar bearing. Figure 19 shows that spray-bar lubrication method is similar to the model for lubricant mixing at a feed groove (section 2.4). A single-orifice feed type is less appropriate because the effects of supply oil churning and heat convection from the pads are not fully modeled.

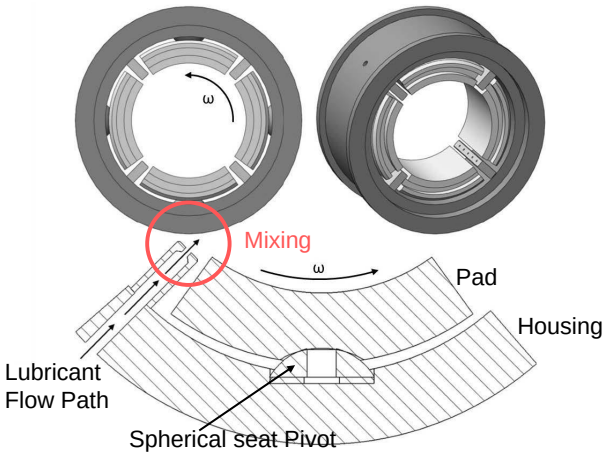

Figure 19: Geometry of spray bar feed type. Original Figure taken from [7].

The thermal mixing coefficient (λ) for the predictions varies with the operating conditions, namely shaft rotational speed. At a high rotor speed, the resistance to supply flow increases and as result the portion of hot oil that is carried over from trailing edge of an upstream pad to leading edge of downstream pad increases. Hence, λ must be modified accordingly. In the following predictions, $\lambda = 0.5, 0.6, 0.7, 0.8$ for operating conditions with rotor speed of 7, 10, 13, 16 kRPM,[8] respectively.

Figure 20 shows the predicted journal eccentricity in the load direction ($-y$) and orthogonal direction (x) compared to the measurements in Ref. [5]. In the load direction, the agreement between prediction and test data worsens by increasing the load and shaft speed. The maximum difference between prediction and test data is 19, 37, and 43 μm for specific loads of $W/(LD) =$ 0.7, 2.1, and 2.9 MPa, respectively. The measured journal eccentricities in the orthogonal direction are larger than the predicted magnitudes; however, the differences are smaller than 20 μm.

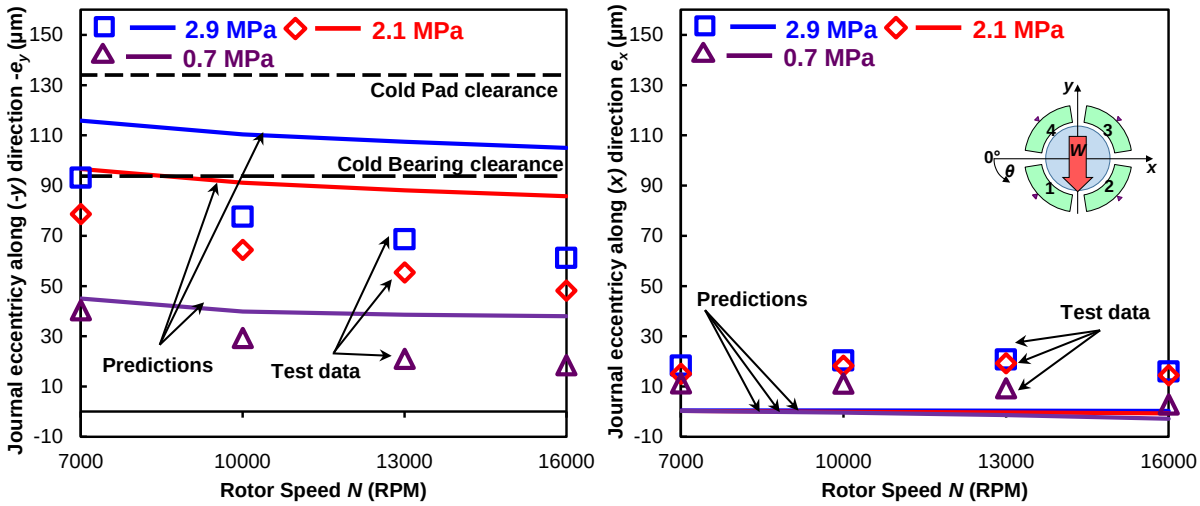

Figure 20: Journal eccentricities ($-e_y, e_x$) versus rotor speed and operation with three specific loads. Predictions and test data in Ref. [5].

Table 4 compares the journal eccentricity along the load direction (e_y) obtained for the TEHD and THD predictions. Predicted journal eccentricity in orthogonal direction (e_x) and the journal attitude angle ($\phi = \tan^{-1}(e_x/e_y)$) are very small and not shown. Predicted journal eccentricity from TEHD analysis is smaller in the load direction compared to the predictions from THD analysis. The TEHD predictions are about 25% smaller than the THD predictions, and correlate better with the test data.

[8] Surface speeds of 38, 53, 69, 85 m/s.

Table 4: TEHD and THD predictions for journal eccentricity in the load direction (e_y) for various specific loads. Predictions compared to test data from Ref. [7]

W/(LD)	0.7 MPa			2.1 MPa			2.9 MPa		
N [RPM]	THD	TEHD	Test	THD	TEHD	Test	THD	TEHD	Test
7000	57.3	45.0	40.3	113.3	96.6	78.6	134.2	115.8	93.1
10000	54.2	39.9	29.3	110.0	91.1	64.4	131.2	110.4	77.6
13000	54.9	38.6	20.9	108.6	88.1	55.3	130.0	107.4	68.5
16000	55.6	38.0	18.4	108.7	85.8	48.2	130.3	105.0	61.1

Figure 21 shows the predicted film temperature rise compared to measured temperature rise on the inner surface of the bearing pads for operation with shaft speed at 16 kRPM in Ref. [5] with an specific load of 0.7, 2.1, and 2.9 MPa. The authors selected (based on industrial practice) the location to measure the maximum temperature at 75% of the pad arc length. Correctly, test results show that the maximum temperatures at this location is greater than the temperature on the pad trailing edge. This is due to the heat convection with the churning cooler oil in the groove region and circumferential heat flow in the pads. Note that the sensor measures the temperature of the solid (pad), not the fluid film. The current prediction model only takes into account the radial heat flow in the pads, hence the maximum temperature prediction happens at the trailing edge.

The agreement of the predictions (TEHD) and the measurements is moderate, the maximum temperature difference is no more than 23%, 27%, 21% for $W/(LD)$ =2.9, 2.1, 0.7 MPa, respectively. As expected, the loaded pads are hotter for operation with a large specific load (2.9 MPa). conversely, the unloaded pads (3, 4) are hotter when operating with a *small* specific load (0.7 MPa). This phenomena appears both in measurements and predictions. For pads 1 and 2, the predicted temperatures are generally higher than the measurements; conversely, the measured temperatures on pads 3 and 4 are higher than the predictions.

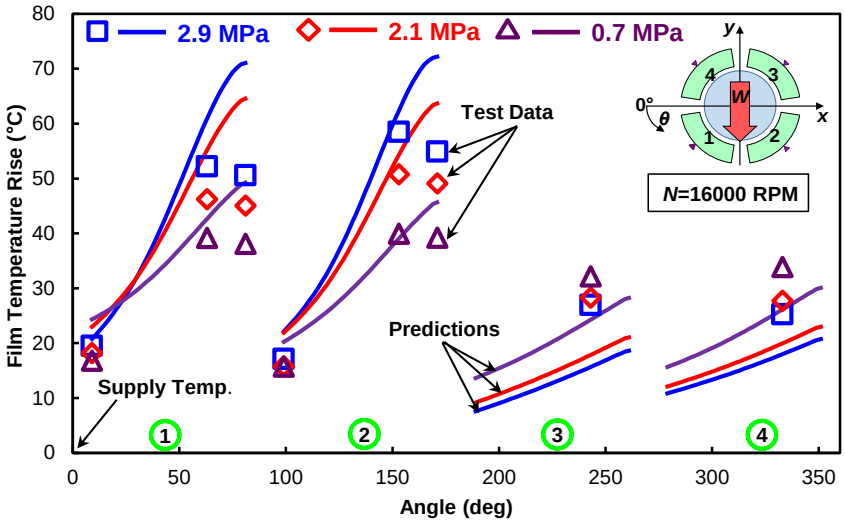

Figure 21: Predicted and measured pad inner surface temperature rise relative to supply temperature (48.9℃). Measured results from Ref. [5]. (*N*=16,000 RPM, *W/(LD)*=2.9, 2.1, 0.7 MPa, and λ=0.8)

For a low rotor speed (7000 RPM), Figure 22 shows the predicted film temperature for the loaded pads is larger than the measured magnitudes, but the predictions for unloaded pads shows a good agreement with test data. For $N = 7000$ RPM the discrepancy is generally smaller than $N = 16000$ RPM.

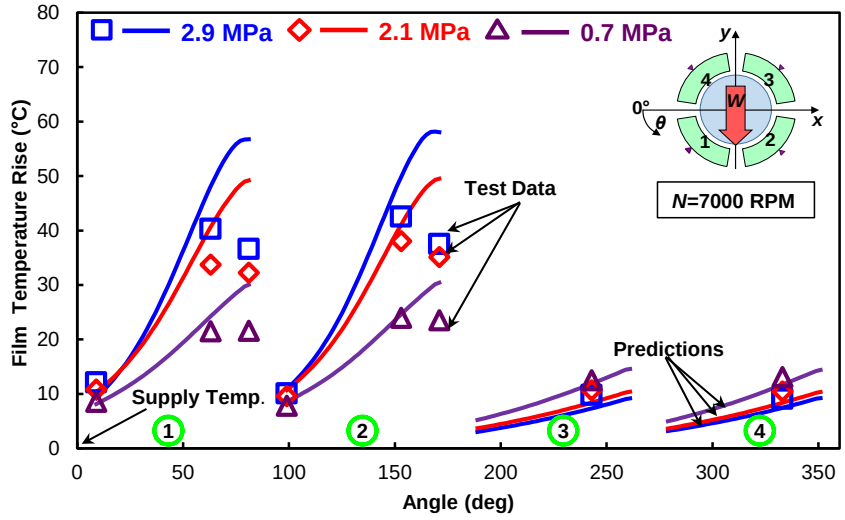

Figure 22: Predicted and measured pads' inner surface temperature rise relative to supply temperature (48.9℃). Measured results from Ref. [5]. (*N*=7,000 RPM, *W/(LD)*=2.9, 2.1, 0.7 MPa, and λ=0.5)

To further study the dependency of the film temperature on the shaft speed, Figure 23 compares the maximum predicted temperature to the measured one for operation under three specific loads. The temperatures increase with an increase in rotor speed and specific load. The

predicted temperatures are larger than the measured ones, but as the specific load decreases the agreement improves. In other words, the agreement of prediction and test data for $W/(LD) = 0.7$ MPa is better than that for 2.1 MPa, which is better than that for 2.9 MPa.

Figure 23 also shows that the predicted maximum pad inner surface temperature increases steadily for higher rotor speeds. The test data follow the same trend, however not as linear. The predicted maximum inner pad temperature for $W/(LD) = 0.7, 2.1, 2.9$ are higher than the test data by 2.8, 9.1, 9.1 °C, respectively.

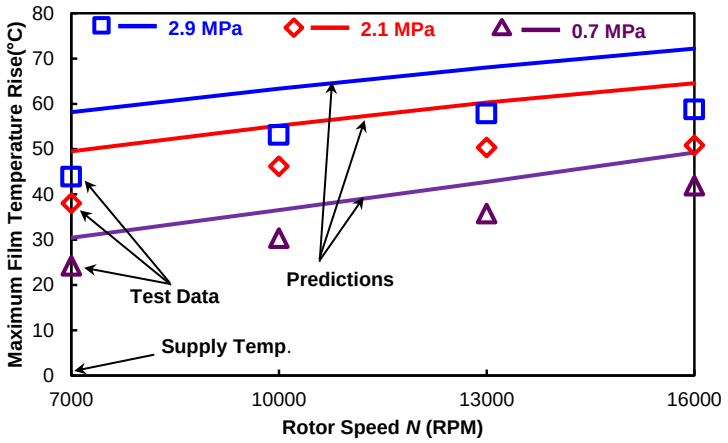

Figure 23: Pad maximum inner surface temperature versus rotor speed and operation with various specific loads. Predictions and test data in Ref. [5]. (*W/(LD)*=2.9, 2.1, 0.7 MPa)

To explain the above trend, Figure 24 shows the predicted flow rate versus the constant flow rate used in the tests (42 LPM). Since the temperature rise is inversely proportional to the flow rate, one can expect higher predicted temperatures when the predicted flow rate is lower than the actual flow rate. The predicted flow rate is mostly below the flow rate used in the tests which justifies the higher predicted temperatures.

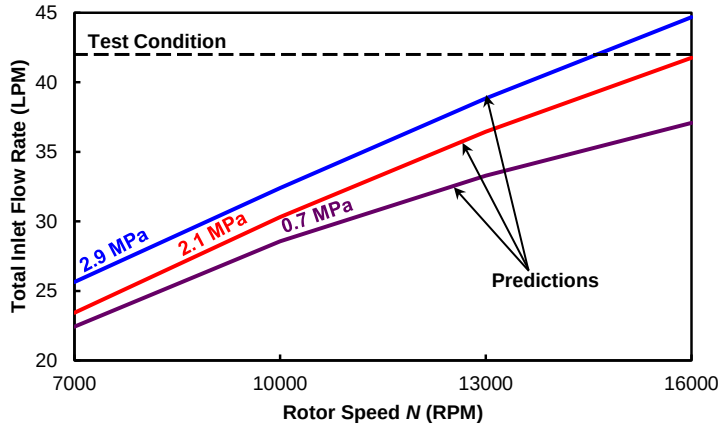

Figure 24: Predicted flow rate versus rotor speed and operation with various specific loads. Constant flow rate in tests [5] for spray-bar with evacuated housing. (*W/(LD)*=2.9, 2.1, 0.7 MPa)

Figure 25 shows the predicted flow on each pad. The majority of the inlet flow is predicted to enter the bearing via the feeding groove on pad 3. Due to the high flow rate of cold (supply) flow, lighter loaded pads (3, 4) remain relatively cold. On the other hand, the amount of flow exiting pad 4 (λQ_4) to enter pad 1 is larger than the predicted leading edge flow (Q_1), so for the equation (15) to hold inlet flow (Q_{supply}) must become negative.

Negative supply flow rate takes place when a steep pressure gradient on the loaded pads induces a more dominant pressure flow than the shear flow, and a portion of lubricant flows in the opposite direction of the shaft rotational speed. This phenomena, however, cannot be explained with the simple model, so in this case the supply flow is set to be zero. No cold supply flow means that all flow that enters pad 1 is warm lubricant from pad 4 which causes over-prediction of its maximum temperature.

In addition, a more uniform pad flow rate for a lower specific load (i.e. 0.7 MPa) explains the better agreement of test data and predictions for a lower specific load in Figure 23.

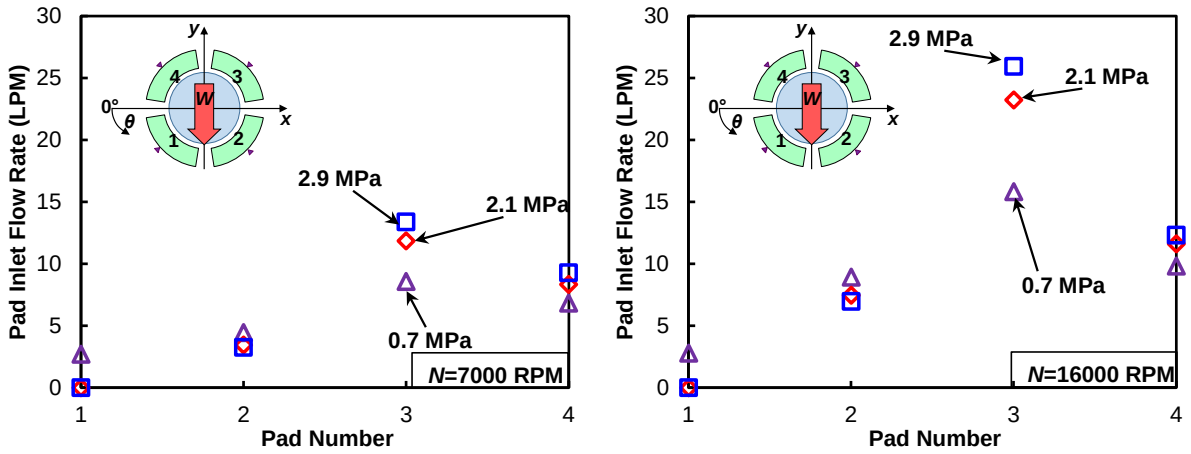

Figure 25: Predicted flow rate on each pad for operation at *N*=7000 and *N*=16000 under various specific loads. ((*W*/(*LD*)=2.9, 2.1, 0.7 MPa)

Coghlan and Childs [5] measured the hot bearing clearance by rolling the shaft on the pads right after shutting down the rotor from a steady state operation. The predicted hot clearances in the (x,y) directions (C_x, C_y) are defined as,

$$C_x = O_{p,x} + \left(R_{in} + u_{(R_{in},\theta)} - R_s - \Delta R_s + \Delta R_h\right)\cos\theta \tag{30a}$$

$$C_y = O_{p,y} + \left(R_{in} + u_{(R_{in},\theta)} - R_s - \Delta R_s + \Delta R_h\right)\sin\theta \tag{30b}$$

Figure 26 shows the predicted hot clearance on each pad surface in agreement with results from Ref. [5]. The agreement between prediction and test data is satisfactory. The clearance of the test bearing has a square shape, the midpoint of each side shows the minimum clearance

(bearing clearance). The corners of the square do not show the hot *pad* clearance. Observe that the predicted minimum clearance is smaller than the measurement for the loaded pads. Since the loaded pads are hotter they have a more pronounced expansion compared to the unloaded pads. The expansion of the pads towards the center of the bearing along with expansion of the journal reduce the bearing clearance.

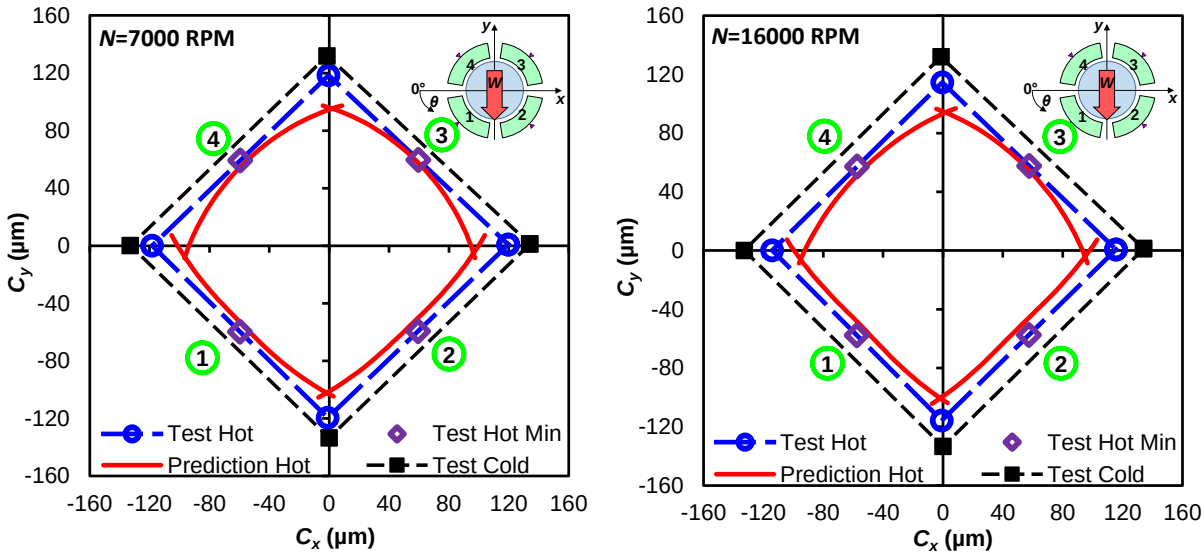

Figure 26: Predicted hot clearance in *x, y* coordinate system compared to test data from Ref. [5]. (*W/(LD)*=2.9 MPa; *Left: N*=7000, *Right: N*=16000)

Figure 27 shows the mean value of the predicted hot bearing clearance versus shaft speed compared to measured estimates. Predictions include thermally and pressure induced pad deformations. Note that pressure deformation does not influence the *bearing* clearance substantially because the pressure induced deformation of the pad is minimum at the pivot location, and the bearing radius is measured at this point. The predictions show a good agreement with test data, with a maximum difference of 6%.

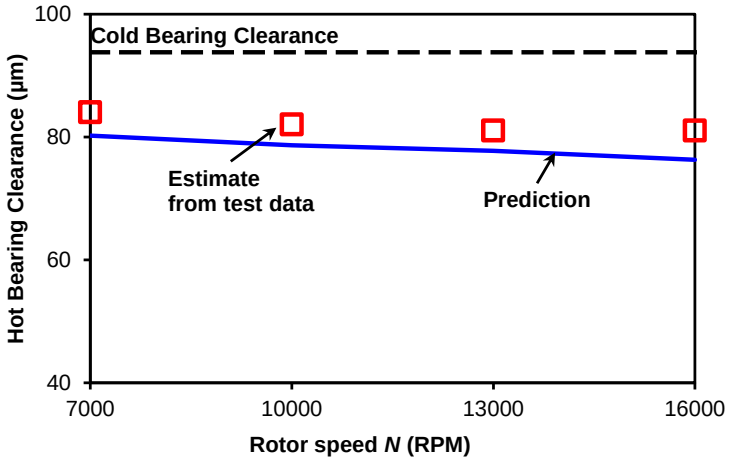

Figure 27: Estimated hot bearing clearance versus rotor speed. Predictions and test data in Ref. [5]. (*W/(LD)*=2.9 MPa)

Figure 28 show the predicted increase in preload ($m = (C_p - C_b)/C_p$) of the pads during the operation. The pad clearance (C_p) increases while the bearing clearance (C_b) decreases (due to the expansion of pad and shaft). The housing installation condition (and direction of expansion) influences the *hot* preload. Predictions account for both thermally and pressure induced deformation of the pads, and the housing is assumed to expand outwards. The preload for loaded pads (1, 2) increases about 100%, and for the unloaded pads (3, 4) it increases about 30%. The higher pressure and higher temperature on the pad 3 and 4 induces a larger pad warping compared to pad 1 and 2.

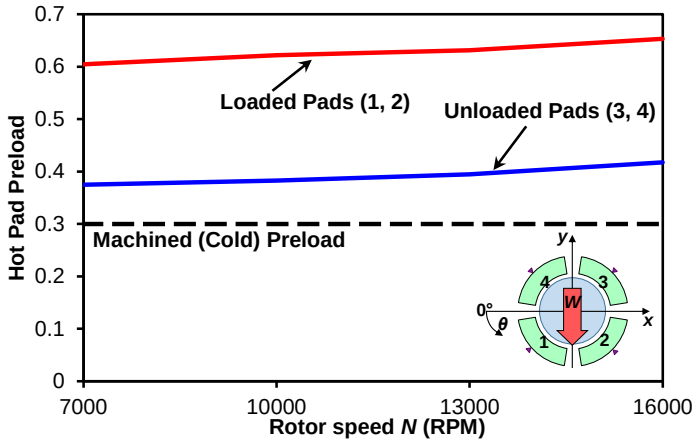

Figure 28: Predicted hot pad preload versus rotor speed for an operation under a specific load of 2.9 MPa

In Ref. [6], Coghlan and Childs use a frequency independent ($[K,C,M]$) model to extract the bearing static stiffness $[K]$, damping $[C]$, and virtual mass $[M]$ coefficients from curve fits

to the experimentally derived complex stiffnesses $[Z]$.

$$\Re(Z) = K - \omega^2 M \text{, and } \quad \Im(Z) = \omega C \tag{31}$$

The measured excitation frequency range is 10 to 250 Hz. Hz. Figures 29 and 30 compare the test data against the THD and TEHD predictions for operation of 7000 RPM and 16000 RPM. The THD prediction only considers pivot flexibility. The right side of the Figures shows the real part of the bearing direct complex stiffnesses ($\Re(Z)$), and the left part shows the imaginary part of the bearing direct complex stiffness ($\Im(Z)$) versus excitation frequency. The results are obtained for operation at three specific loads, $W/(LD)$=0.7, 2.1, 2.9 MPa.

In general, TEHD predictions improve the agreement with the test data, except for the case with $N = 16000$ RPM and $W/(LD) = 0.7$ MPa. Since the predictions are the same along x and y directions, and under-predict the test data, they correlate best with real and imaginary part of Z_{xx}. The agreement of the imaginary part of the bearing direct complex stiffness ($\Im(Z)$) is best for lowest specific load (0.7 MPa) for both shaft speeds (7000 and 16000 RPM). Conversely, the agreement of the real part of the bearing direct complex stiffness ($\Re(Z)$) is best for highest specific load (2.9 MPa) for both shaft speeds (7000 and 16000 RPM).

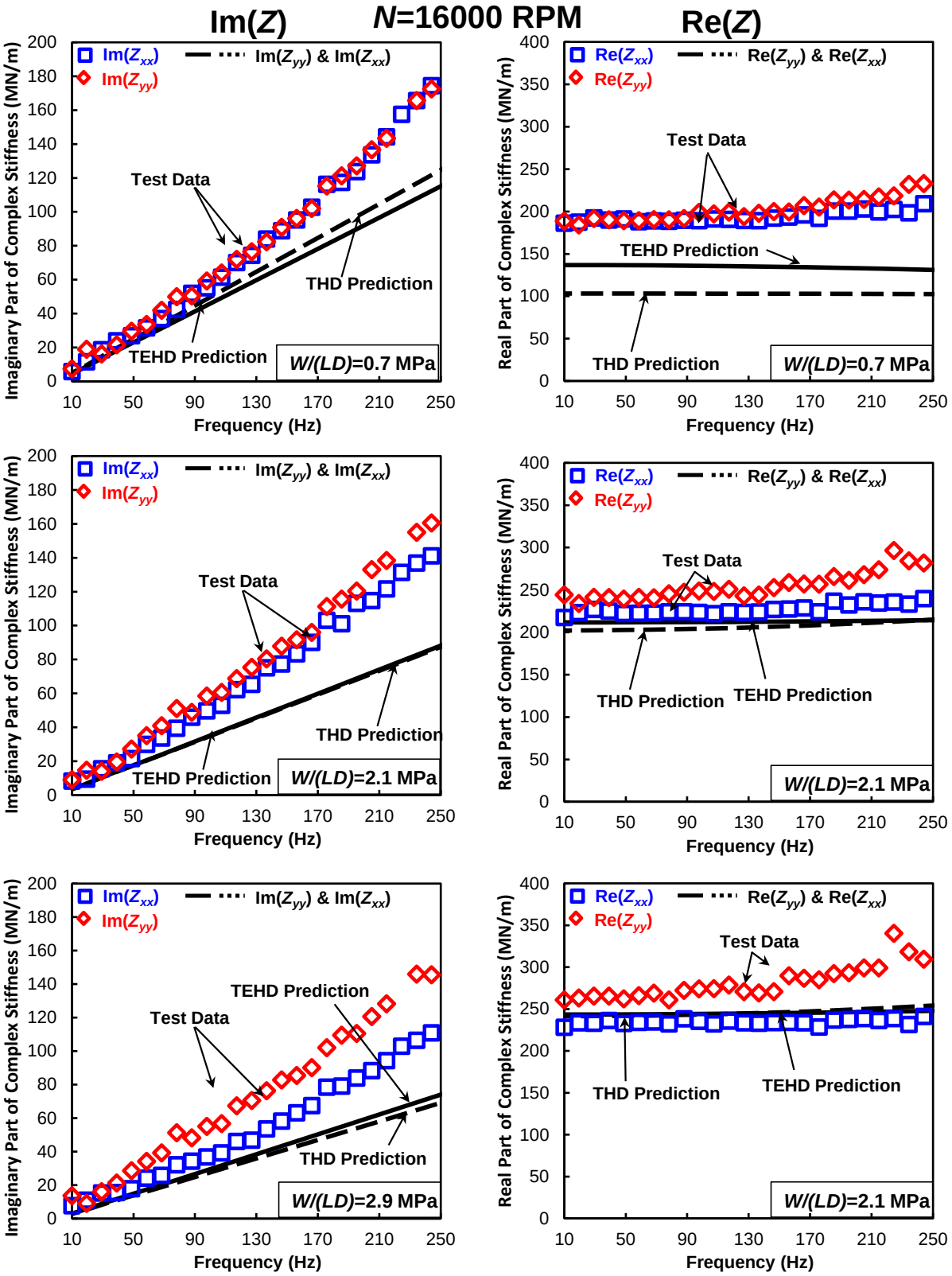

Figure 29: Imaginary (left) and Real (right) part of complex bearing stiffness versus excitation frequency for operation at various specific loads. TEHD and THD predictions compared to measurements in Ref. [6] for operation of *N*=16000, and *W/(LD)*=0.7, 2.1, and 2.9 MPa

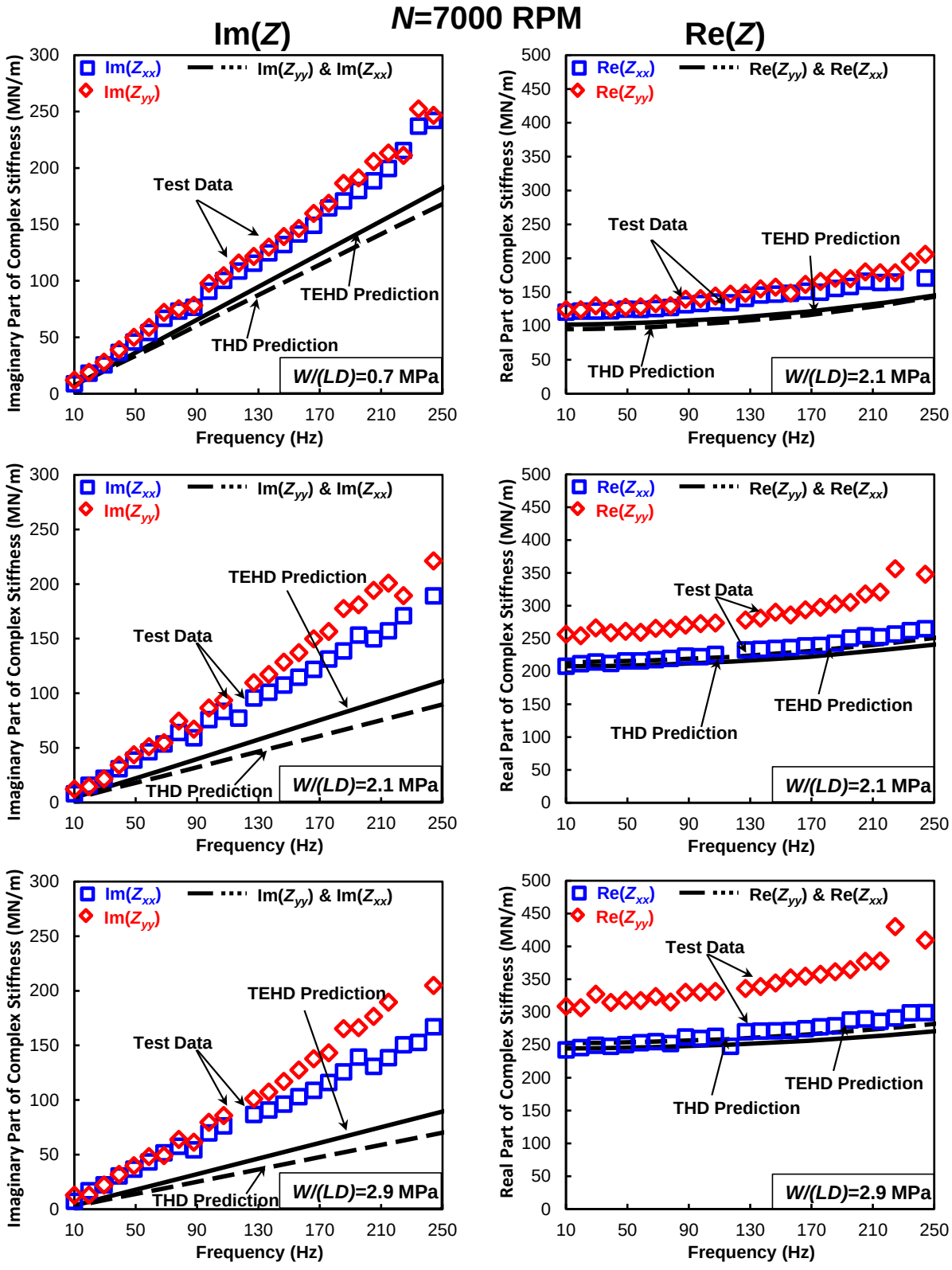

Figure 30: Imaginary (left) and Real (right) part of complex bearing stiffness versus excitation frequency for operation at various specific loads. TEHD and THD predictions compared to measurements in Ref. [6] for operation of N=7000, and $W/(LD)$=0.7, 2.1, and 2.9 MPa

As per the rotordynamic coefficients, Figure 31 and 32 show predicted synchronous speed reduced force coefficients from a $[K,C,M]$ model. TEHD predictions for K_{yy}, K_{xx} are in a very good agreement with the measurements with a maximum difference less than 27%. However, the current model predicts isotropic stiffness for the bearing, but the test data show stiffness orthotropy which is not expected for the LBP configuration as much as for a LOP configuration.

In addition, observe that at the specific load of 0.7 MPa, the TEHD predictions are larger than THD predictions, but at 2.1 MPa the TEHD predictions become smaller than THD predictions. At a low specific load (0.7 MPa), the thermally induced deformation is dominant and the thermal expansion of the bearing components reduces the film thickness and makes the bearing stiffer. At a high specific load (2.9 MPa), the pressure induced pad deformation is dominant, and the elastic opening of the pad slightly increases the film thickness, and the stiffness becomes slightly lower than that of the THD prediction.

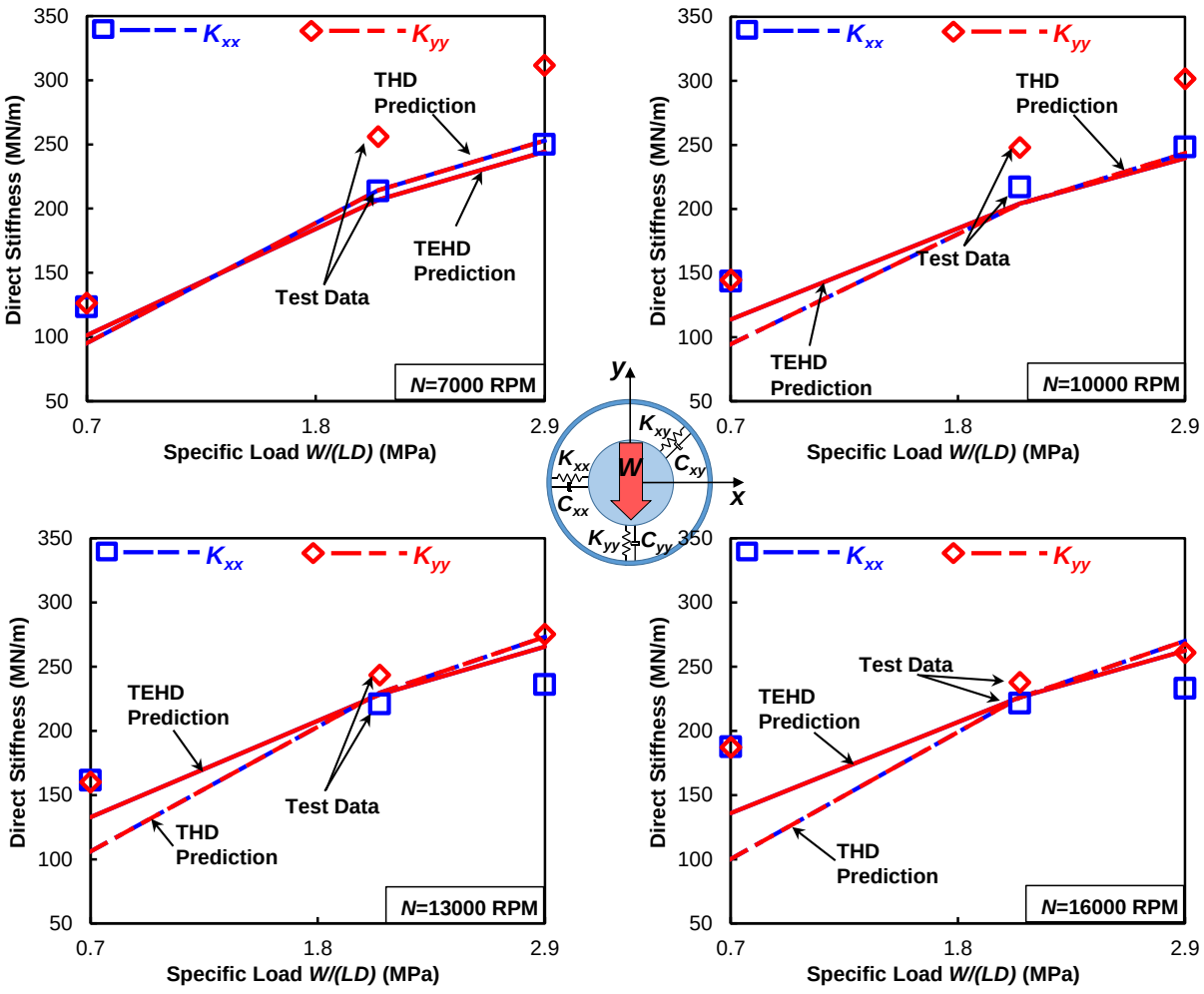

Figure 31: Direct stiffness coefficients (K_{yy}, K_{xx}) versus specific load for operation at four shaft speeds. TEHD and THD prediction and test data from Ref. [6] (Synchronous speed excitation)

Figure 32 shows predicted damping coefficients (C_{xx}, C_{yy}) in comparison with the estimation from test data. Compared to stiffness, the predicted damping shows a more considerable discrepancy with the measurements. In a $[K,C]$ model, including the thermally and pressure induced deformations reduces the predicted damping [12]. However, current predictions (with a $[K,C,M]$ model) show that, although not significant, TEHD analysis predicts a higher damping and has a better agreement with test results compared to THD predictions. The difference between TEHD predictions and test data range between 27% and 52%.

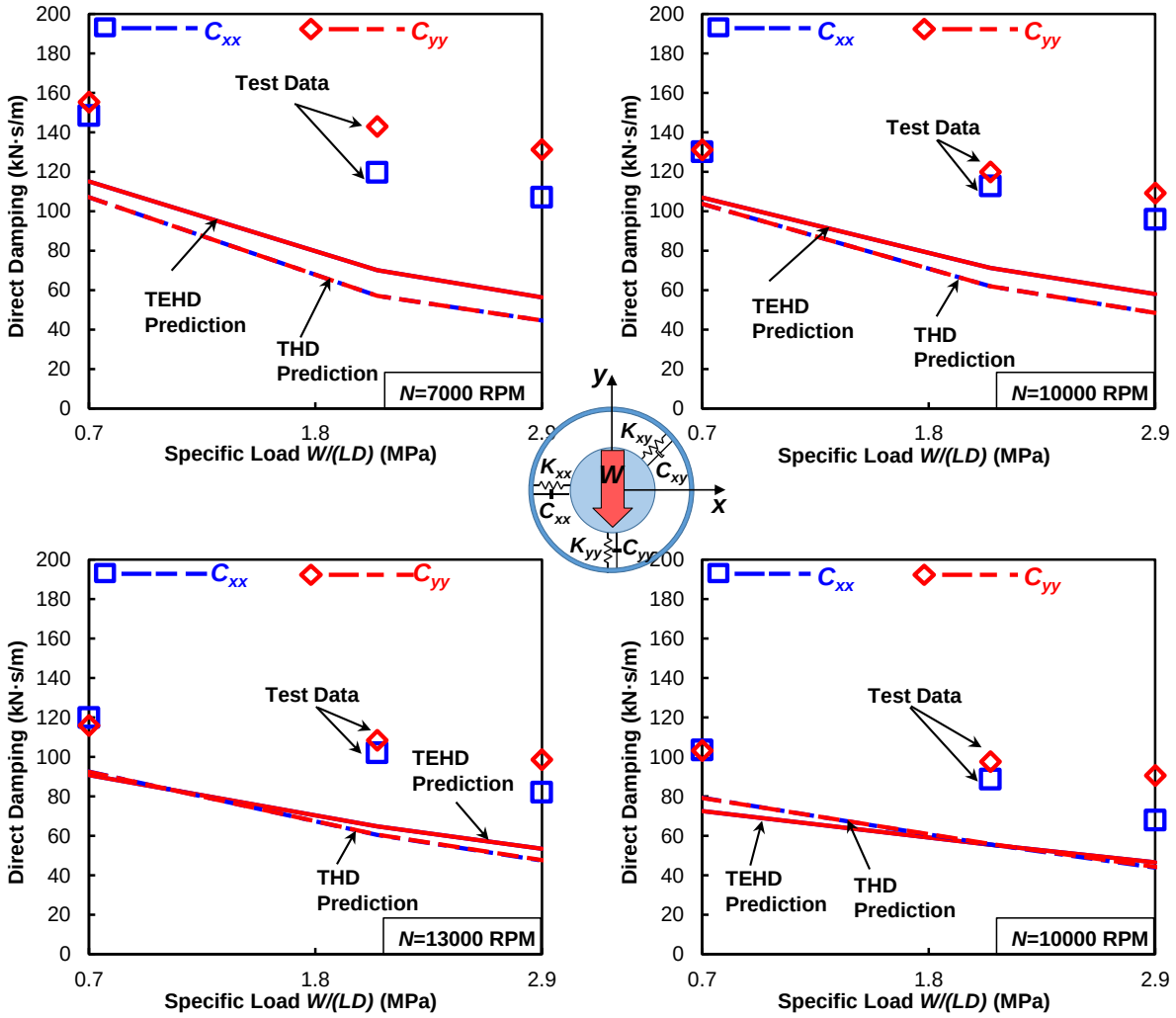

Figure 32: Direct damping coefficients (C_{yy}, C_{xx}) versus specific load for operation at four shaft speeds. TEHD and THD prediction and test data from Ref. [6] (Synchronous speed excitation))

CONCLUSION

The aim of the presented work is to implement a method to include thermal effects on tilting pad journal bearings (TPJBs) in a predictive tool (XLTPJB®). An important objective of the project is to have a *fast* and *reliable* predictive tool that can help design and analyze TPJBs with accuracy. In order to do so, authors preformed an extensive literature review to study the practiced methods that account for the thermally induced deformations of TPJB components, with a focus on deformation of the pads.

Due to a lack of accurate knowledge of the thermal boundary conditions on a TPJB pad, authors decided to pursue a simple but physically sound model for temperature as opposed to complex finite element methods that would heavily rely on assumptions for boundary condition . The temperature field in a pad is considered to be solely a function of radius across the pad thickness, which allows for using existing empirical correlations to find the convection coefficients on inner surface and back of the pad. These convection coefficients will determine the heat flow in and out of the pad and are paramount to calculation of inner surface and back surface temperatures.

The early computational models calculate the pad thermally induced deformation by assuming the pad as a straight or a curved beam. Subsequently, apply a moment equivalent to the temperature gradient on the pads to find their thermal warping. To find the expansions, the models use a simple linear expansion formula for the pad thickness. More recent models use FEM to find the thermoelastic deformations of a pad given the temperature field in the pad.

The current work pursue basic methods from theory of elasticity to derive an explicit formula for the pad mid-plane thermal deformation than works as well as a 2D finite element model for the same (radial) temperature field. The radial and circumferential deformation vectors of a pad are found from the thermally induced strains in a pad, neglecting the thermally induced stresses. Thermal stresses are shown to be not important to the resultant deformation.

For the axial warping of the pad, a simple beam cantilevered at the mid-plane represents the pad in the axial direction. The deformation field along the radial direction then can be expressed by super-imposing the deformation of circumferential and axial cross sections which approximates 3D FEM result for the same temperature field with less than 20% difference. Note that in the current model 3D effects are not accounted for, and the deformation of the mid plane is identical to 2D FEM results.

To check the accuracy of the model, the authors compare the predictions with the measurements of two independent, recent (2013, 2014) test programs for evaluating the performance characteristics of TPJBs. In the first case, Hagemann et al. [4] measure the dynamic and static characteristics of a large size (shaft radius of 0.5 m) 5 pad LBP TPJB under heavy loads (spe-

cific loads of 1 to 2.5 MPa). The current TEHD model predicts the temperature of pad inner surface, hydrodynamic pressure, and film thickness with a good agreement to the test data. The TEHD model reduces the discrepancy of THD prediction and test data for peak pressure by 14%, maximum temperature by 11%, and minimum film thickness by 56%. Along the axial direction, the simple beam model provides good correlation for film thickness and pressure distribution.

The current model predicts $[K,C]$ direct rotordynamic coefficients that have a smaller discrepancy with the test data compared to the predictions by Hagemann et al. [4]. The predicted rotordynamic coefficients along the load direction have a better agreement with test data with difference between 12% and 34% for K_{yy} and betweem 1% and 49% for C_{yy}. Hagemann et al. [4] believe that the major reason for their prediction discrepancy is neglecting inertia in their analysis.

The second case from Coghlan and Childs [5, 6, 7] studies the effect of various direct lubrication methods on the performance of a 4 pad LBP TPJBs. This test program provides very detailed measurements to compare the predictions against test data for a spherical seat TPJB with spray bar lubrication under specific loads between 0.7 and 2.9 MPa and surface speeds between 38 and 85 m/s.

The predicted pad inner surface temperatures are consistently larger (no more than 18% difference) than the measured ones which is related to the fact that the tests are performed in over-flooded bearing condition (as recommended by the test bearing OEM). The predicted shaft eccentricities has a moderate agreement with the measured ones, the predictions are larger in the load direction and smaller in the orthogonal direction. The predicted hot clearances are closely predicted with maximum difference of 6% for a specific load of 2.9 MPa and various shaft speeds. The predicted hot pad preload can increase up to 100% during the operation.

Coghlan and Childs [6] measure complex impedances of the bearing to study the frequency dependency of this bearing, and use a $[K,C,M]$ model to represent the stiffness, damping, and inertia of the bearing. The predicted stiffness with the $[K,C,M]$ model has a very good agreement with the test data, with a maximum difference of 27%. The TEHD model improves THD predictions for stiffness coefficients, especially at lower specific load (0.7 MPa). The predicted damping coefficients are consistently smaller than the measured ones for analysis. The predictions from TEHD model differed with the test data in a range between 27% and 52%, and had a slightly better agreement with the measured ones compared to the prediction from THD model.

The authors observed a similar trend in both comparison cases which relates the bearing flow rate and predicted temperatures. The current model in XLTPJB® assumes that the bearing is flooded. However, in the first case the bearing is starved, leading to a considerable under-

prediction of film temperature for unloaded pads, and in the second case the bearing is over-flooded leading to over-prediction of film temperature for loaded pads. It is vital to be able to impose the flow rate used in the test rig or industrial practice to get accurate film temperature, which effects the TPJB performance substantially through modifying lubricant viscosity.

REFERENCES

[1] San Andrés, L., and Tao, Y., 2013, "The Role of Pivot Stiffness on the Dynamic Force Coefficients of Tilting Pad Journal Bearings," ASME J. Eng. Gas Turb. Pow., **135**(11), p. 112505.

[2] San Andrés, L., Tao, Y., and Li, Y., 2015, "Tilting Pad Journal Bearings: On Bridging the Hot Gap Between Experimental Results and Model Predictions," ASME J. Eng. Gas Turb. Pow., **137**(2), p. 022505.

[3] San Andrés, L., and Li, Y., 2015, "Effect of Pad Flexibility on the Performance of Tilting Pad Journal Bearings–Benchmarking a Predictive Model," ASME J. Eng. Gas Turb. Pow., **137**(12), p. 122503.

[4] Hagemann, T., Kukla, S., and Schwarze, H., 2013, "Measurement and Prediction of the Static Operating Conditions of a Large Turbine Tilting-Pad Bearing Under High Circumferential Speeds and Heavy Loads," ASME Turbo Expo 2013: Turbine Technical Conference and Exposition, pp. V07BT30A019–V07BT30A019.

[5] Coghlan, D. M., and Childs, D. W., 2015, "Characteristics of a Spherical Seat TPJB With Four Methods of Directed Lubrication: Part 1–Thermal and Static Performance," ASME Turbo Expo 2015: Turbine Technical Conference and Exposition, pp. V07AT31A003–V07AT31A003.

[6] Coghlan, D. M., and Childs, D. W., 2015, "Characteristics of a Spherical Seat TPJB With Four Methods of Directed Lubrication: Part 2–Rotordynamic Performance," ASME Turbo Expo 2015: Turbine Technical Conference and Exposition, pp. V07AT31A003–V07AT31A003.

[7] Coghlan, D. M., 2014, "Static, Rotordynamic, and Thermal Characteristics of a Four Pad Spherical-Seat Tilting Pad Journal Bearing with Four Methods of Directed Lubrication," Masters thesis, Texas A&M University.

[8] Ettles, C. M., 1980, "The Analysis and Performance of Pivoted Pad Journal Bearings Considering Thermal and Elastic Effects," ASME J. Lubr. Technol., **102**(2), pp. 182–191.

[9] Ferron, J., Frene, J., and Boncompain, R., 1983, "A Study of the Thermohydrodynamic Performance of a Plain Journal Bearing Comparison Between Theory and Experiments," ASME J. Lubr. Technol., **105**(3), pp. 422–428.

[10] Boncompain, R., Fillon, M., and Frene, J., 1986, "Analysis of Thermal Effects in Hydrodynamic Bearings," ASME J. Tribol., **108**(2), pp. 219–224.

[11] Lund, J. W., and Pedersen, L. B., 1987, "The Influence of Pad Flexibility on the Dynamic Coefficients of a Tilting Pad Journal Bearing," ASME J. Tribol., **109**(1), pp. 65–70.

[12] Brugier, D., and Pascal, M. T., 1989, "Influence of Elastic Deformations of Turbo-Generator Tilting Pad Bearings on the Static Behavior and on the Dynamic Coefficients in Different Designs," ASME J. Tribol., **111**(2), pp. 364–371.

[13] Wilcock, D. F., and Booser, E. R., 1990, "Thermal Behavior in Tilting Pad Journal Bearings," STLE Tribol. Trans., **33**(2), pp. 247–253.

[14] Fillon, M., Souchet, D., and Frêne, J., 1990, "Influence of Bearing Element Displacements on Thermohydrodynamic Characteristics of Tilting-Pad Journal Bearings," Proc. Japan International Tribology Conference, Nagoya, pp. 635–640.

[15] Brockwell, K., and Dmochowski, W., 1992, "Thermal Effects in the Tilting Pad Journal Bearings," Journal of Physics D: Applied Physics, **25**(3), p. 384.

[16] He, M., 2003, "Thermoelastohydrodynamic Analysis of Fluid Film Journal Bearings," PhD thesis, University of Virginia, Charlottesville, VA, USA.

[17] Kukla, S., Hagemann, T., and Schwarze, H., 2013, "Measurement and Prediction of the Dynamic Characteristics of a Large Turbine Tilting-Pad Bearing Under High Circumferential Speeds," ASME Turbo Expo 2013: Turbine Technical Conference and Exposition, pp. V07BT30A020–V07BT30A020.

[18] Desbordes, H., Fillon, M., Frene, J., and Wai, C. C. H., 1995, "The Effects of Three-Dimensional Pad Deformations on Tilting-Pad Journal Bearings Under Dynamic Loading," ASME J. Tribol., **117**(3), pp. 379–384.

[19] Suh, J., and Palazzolo, A., 2014, "Three-Dimensional Thermohydrodynamic Morton Effect SimulationPart I: Theoretical Model," ASME J. Tribol., **136**(3), p. 031706.

[20] Suh, J., and Palazzolo, A., 2014, "Three-Dimensional Thermohydrodynamic Morton Effect AnalysisPart II: Parametric Studies," ASME J. Tribol., **136**(3), p. 031707.

[21] Kulhanek, C. D., and Childs, D. W., 2012, "Measured Static and Rotordynamic Coefficient Results for a Rocker-Pivot, Tilting-Pad Bearing With 50 and 60% Offsets," ASME J. Eng. Gas Turb. Pow., **134**(5), p. 052505.

[22] Wodtke, M., Fillon, M., Schubert, A., and Wasilczuk, M., 2013, "Study of the Influence of Heat Convection Coefficient on Predicted Performance of a Large Tilting-Pad Thrust Bearing," ASME J. Tribol., **135**(2), p. 021702.

[23] San Andrés, L., 2012, Modern Lubrication Theory, Notes 10: Thermohydrodynamic Bulk-Flow Model in Thin Film Lubrication, `http://hdl.handle.net/1969.1/93250`. [Online; accessed April 2016].

[24] San Andrés, L., and Kim, T. H., 2010, "Thermohydrodynamic Analysis of Bump Type Gas Foil Bearings: A Model Anchored to Test Data," ASME J. Eng. Gas Turb. Pow., **132**(4), p. 042504.

[25] Hausen, H., 1959, "Neue gleichungen für die wärmeübertragung bei freier und erzwungener strömung," Allg. Wärmetech, **9**(4), p. 5.

[26] Gnielinski, V., 2009, "Heat Transfer Coefficients for Turbulent Flow in Concentric Annular Ducts," Heat Transfer Engineering, **30**(6), pp. 431–436.

[27] Boley, B. A., and Weiner, J. H., 1960, *Theory of Thermal Stresses,* John Wiley and Sons Inc., pp. 244-249.

[28] Timoshenko, S. P., and Goodier, J. N., 1970, *Theory of Elasticity*, third ed. McGraw-Hill, pp. 75-80.

[29] Boley, B. A., and Barrekette, E. S., 1958, "Thermal Stresses in Curved Beams," J. of Aero Space Sciences, **25**(210), pp. 627–630.

[30] Hetnarski, R. B., Eslami, M. R., and Gladwell, G., 2009, *Thermal Stresses: Advanced Theory and Applications*, Vol. 41 Springer, pp. 227-231.

A. APPENDIX: THERMAL STRESSES

This appendix briefly explains the method in Ref. [29] adjusted for a bearing pad. Consider a curved beam of rectangular cross section and with constant properties, under a temperature $\bar{T}$ varying only in the radial direction. Thermal stress in local radial (σ_r) and circumferential ($\sigma_{\hat{\theta}}$) from theory of elasticity is [29]

$$\sigma_r = \frac{A_1}{r^2} + \frac{A_2}{{R_{in}}^2}\left(2\ln\left(r/R_{in}\right)+1\right) + 2\frac{A_3}{{R_{in}}^2} - \frac{E\alpha}{r^2}\int_{R_{in}}^{r}\bar{T}rdr \tag{A.1a}$$

$$\sigma_{\hat{\theta}} = -\frac{A_1}{r^2} + \frac{A_2}{{R_{in}}^2}\left(2\ln\left(r/R_{in}\right)+3\right) + 2\frac{A_3}{{R_{in}}^2} - E\alpha\left[\bar{T} - \left(1/r^2\right)\int_{R_{in}}^{r}\bar{T}rdr\right] \tag{A.1b}$$

Let $r_0 = R_{out}/R_{in}$, in Eq. (A.1) the constants N, A_1, A_2, A_3 are specified as [29]

$$N = 4r_0^2(\ln r_0)^2 - (r_0^2-1)^2 \tag{A.2a}$$

$$A_1 = \frac{E\alpha}{N}\left(\left[2r_0^2\ln(r_0)[2\ln(r_0)-1]+r_0^2-1\right]\int_{R_{in}}^{R_{out}}\bar{T}rdr - 4r_0^2\ln(r_0)\int_{R_{in}}^{R_{out}}\bar{T}r\ln(r/R_{in})dr\right) \tag{A.2b}$$

$$A_2 = \frac{E\alpha}{N}\left(\left[2r_0^2\ln(r_0)-r_0^2+1\right]\int_{R_{in}}^{R_{out}}\bar{T}rdr - 2[r_0^2-1]\int_{R_{in}}^{R_{out}}\bar{T}r\ln(r/R_{in})dr\right) \tag{A.2c}$$

$$A_3 = \frac{E\alpha}{N}\left(-2r_0^2[\ln(r_0)]^2\int_{R_{in}}^{R_{out}}\bar{T}rdr + \left[2r_0^2\ln(r_0)+r_0^2-1\right]\right]\int_{R_{in}}^{R_{out}}\bar{T}r\ln(r/R_{in})dr\right) \tag{A.2d}$$

For the following Figures, the geometry and temperature boundary conditions are the same as those used for Figure 7. The inner radius of the pad (R_{in}) is 0.051 m, the outer radius (R_{out}) is 0.07 m. The pad thermal expansion coefficient (α) is 1.3×10^{-5} 1/°C, and temperature boundary conditions for inner and outer surfaces are respectively $\bar{T}_{in} = 80°\text{C}, \bar{T}_{out} = 72°\text{C}$.

Figure 33 shows the radial and circumferential stresses due to the temperature gradient across the thickness for the test pad in Ref. [5]. Note that circumferential stresses are much larger than the radial stresses.

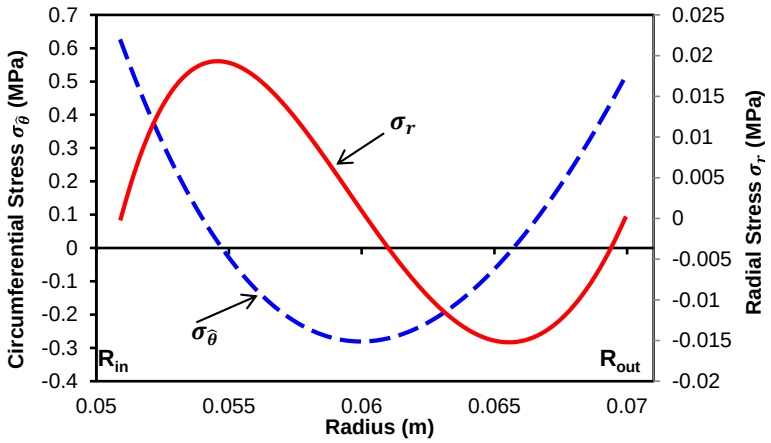

Figure 33: Thermally induced stress along the circumferential and radial direction for a test pad in Ref. [5].

The strains from the generalized Hooke's law read,

$$\varepsilon_r = \frac{-\nu\,\sigma_{\hat{\theta}} + \sigma_r}{E} + \alpha\,\Delta\bar{T} \tag{A.3a}$$

$$\varepsilon_{\hat{\theta}} = \frac{-\nu\,\sigma_r + \sigma_{\hat{\theta}}}{E} + \alpha\,\Delta\bar{T} \tag{A.3b}$$

For the steel pads, the elasticity modulus is very large, so the first term on the right hand side of Eq. (A.3) which is due to the thermal stresses is negligible. For the example test bearing in Ref. [5], elasticity modulus (E) is 2.05×10^{11}, so on the right hand side, the order of magnitude for the first term is 10^{-7}, while for the second term it is 10^{-4}.

Figure 34 shows that the thermal stress contribution to strains in radial and circumferential directions are negligible, and justifies neglecting the stress terms, allowing the use of the separation of variables method in section 2.5.

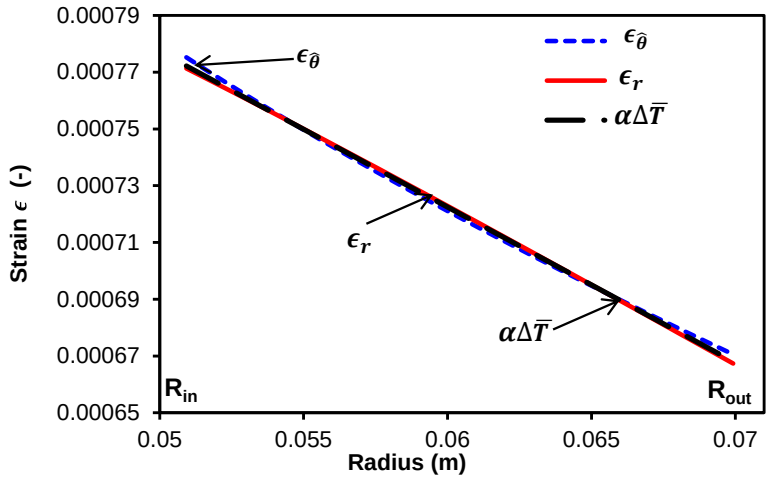

Figure 34: Comparison of thermal strain with and without considering thermally induced stress along the circumferential and radial direction for a test pad in Ref. [5].

Figure 35 illustrates the pad inner surface deformation along the radial direction versus pad local angle ($\hat{\theta}$), and compares the current method result to 2D FEM. The deformation from the current method is almost identical to the FEM result which includes the thermal stress. This justifies the accuracy of the assumption to neglect the stresses.

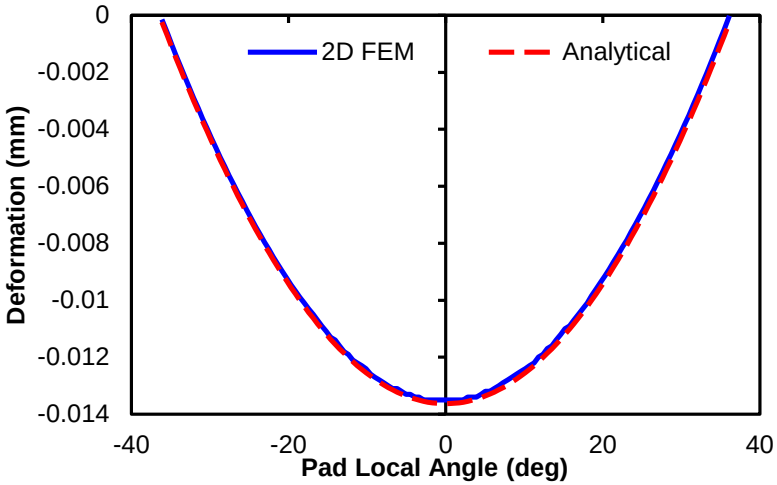

Figure 35: Pad inner surface deformation along the radial direction versus pad local angle ($\hat{\theta}$). Current method results compared to 2D FEM for a test pad in Ref. [5].